Cell

p53 is a central regulator driving neurodegeneration caused by *C9orf72* poly(PR)

Graphical Abstract

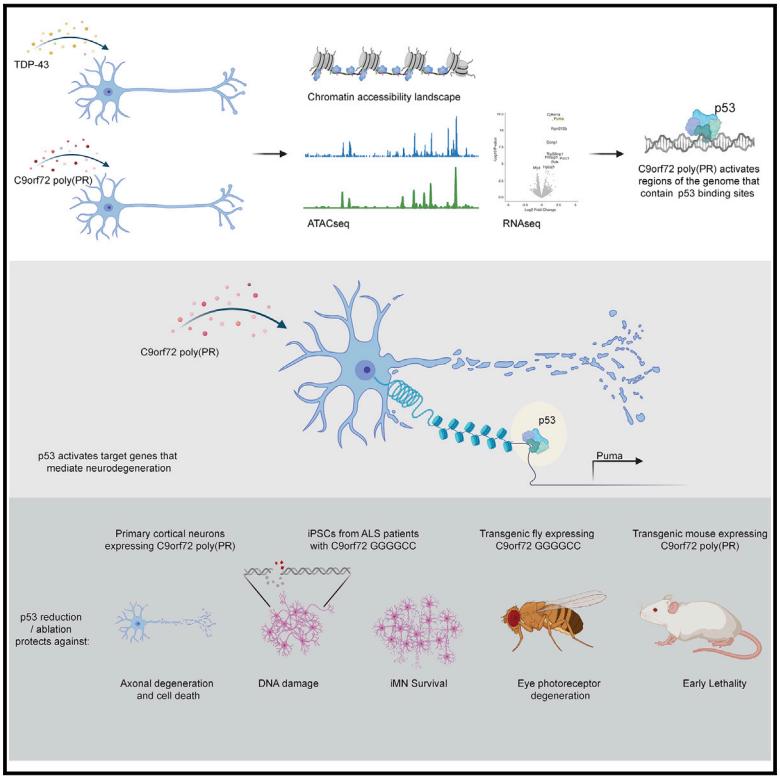

Highlights

- ATAC-seq reveals a chromatin accessibility signature activated by *C9orf72* poly(PR)
- *C9orf72* poly(PR) leads to p53 stabilization and transcription of p53 target genes
- p53 ablation protects against neurodegeneration in multiple *C9orf72* models

Authors

Maya Maor-Nof, Zohar Shipony, Rodrigo Lopez-Gonzalez, ..., Jennifer S. Yokoyama, Leonard Petrucelli, Aaron D. Gitler

Correspondence

maormaya@stanford.edu (M.M.-N.), agitler@stanford.edu (A.D.G.)

In Brief

C9orf72 mutations associated with ALS and FTD activate a specific transcriptional program that converges on p53 to drive neurodegeneration in multiple *C9orf72* models.

Maor-Nof et al., 2021, Cell *184*, 689–708
February 4, 2021
https://doi.org/10.1016/j.cell.2020.12.025

CellPress

Cell

CellPress

Article

p53 is a central regulator driving neurodegeneration caused by *C9orf72* poly(PR)

Maya Maor-Nof,[1,*] Zohar Shipony,[1] Rodrigo Lopez-Gonzalez,[2,10] Lisa Nakayama,[1] Yong-Jie Zhang,[3] Julien Couthouis,[1] Jacob A. Blum,[1] Patricia A. Castruita,[4] Gabriel R. Linares,[5] Kai Ruan,[6] Gokul Ramaswami,[7] David J. Simon,[8,11] Aviv Nof,[1] Manuel Santana,[5] Kyuho Han,[1] Nasa Sinnott-Armstrong,[1] Michael C. Bassik,[1] Daniel H. Geschwind,[7] Marc Tessier-Lavigne,[8] Laura D. Attardi,[1,9] Thomas E. Lloyd,[6] Justin K. Ichida,[5] Fen-Biao Gao,[2] William J. Greenleaf,[1] Jennifer S. Yokoyama,[4] Leonard Petrucelli,[3] and Aaron D. Gitler[1,12,*]

[1]Department of Genetics, Stanford University School of Medicine, Stanford, CA, USA
[2]Department of Neurology, University of Massachusetts Medical School, Worcester, MA, USA
[3]Department of Neuroscience, Mayo Clinic, Jacksonville, FL, USA
[4]Memory and Aging Center, Department of Neurology, University of California, San Francisco, San Francisco, CA, USA
[5]Department of Stem Cell Biology and Regenerative Medicine, Eli and Edythe Broad Center for Regenerative Medicine and Stem Cell Research, University of Southern California, Los Angeles, CA, USA
[6]Department of Neurology, Solomon H. Snyder Department of Neuroscience, School of Medicine, Johns Hopkins University, Baltimore, MD, USA
[7]Department of Neurology, Program in Neurogenetics, David Geffen School of Medicine, University of California, Los Angeles, Los Angeles, CA, USA
[8]Department of Biology, Stanford University, Stanford, CA, USA
[9]Division of Radiation and Cancer Biology, Department of Radiation Oncology, Stanford University School of Medicine, Stanford, CA, USA
[10]Present address: Department of Neurosciences, Lerner Research Institute, Cleveland Clinic, Cleveland, OH 44195, USA
[11]Present address: Department of Biochemistry, Weill Cornell Medical College, New York, NY, USA
[12]Lead contact
*Correspondence: maormaya@stanford.edu (M.M.-N.), agitler@stanford.edu (A.D.G.)
https://doi.org/10.1016/j.cell.2020.12.025

SUMMARY

The most common genetic cause of amyotrophic lateral sclerosis (ALS) and frontotemporal dementia (FTD) is a GGGGCC repeat expansion in the *C9orf72* gene. We developed a platform to interrogate the chromatin accessibility landscape and transcriptional program within neurons during degeneration. We provide evidence that neurons expressing the dipeptide repeat protein poly(proline-arginine), translated from the *C9orf72* repeat expansion, activate a highly specific transcriptional program, exemplified by a single transcription factor, p53. Ablating p53 in mice completely rescued neurons from degeneration and markedly increased survival in a *C9orf72* mouse model. p53 reduction also rescued axonal degeneration caused by poly(glycine-arginine), increased survival of *C9orf72* ALS/FTD-patient-induced pluripotent stem cell (iPSC)-derived motor neurons, and mitigated neurodegeneration in a *C9orf72* fly model. We show that p53 activates a downstream transcriptional program, including *Puma*, which drives neurodegeneration. These data demonstrate a neurodegenerative mechanism dynamically regulated through transcription-factor-binding events and provide a framework to apply chromatin accessibility and transcription program profiles to neurodegeneration.

INTRODUCTION

Amyotrophic lateral sclerosis (ALS) and frontotemporal dementia (FTD) are two devastating neurodegenerative diseases. ALS is a motor neuron disease associated with motor impairments and paralysis, while FTD is associated with cognitive and behavioral impairments. Both diseases share some clinical overlap and also similar neuropathology, including aggregation of the RNA-binding protein TDP-43 in the brain and spinal cord of affected individuals (Neumann et al., 2006). The two diseases are also linked by genetics, including a mutation in the *C9orf72* gene as the most common cause of both FTD and ALS (DeJesus-Hernandez et al., 2011; Renton et al., 2011).

The *C9orf72* mutation is a large GGGGCC repeat expansion in the first intron of the gene. There are several different ways by which this mutation might cause disease (Gitler and Tsuiji, 2016; Ling et al., 2013). One way is by loss of function, resulting from decreased *C9orf72* expression (DeJesus-Hernandez et al., 2011; Kim et al., 2020). Another way is by the accumulation of GGGGCC-containing RNAs (and GGCCCC RNAs produced from the antisense transcript) that sequester critical RNA-binding proteins (Cooper-Knock et al., 2014; Donnelly et al., 2013;

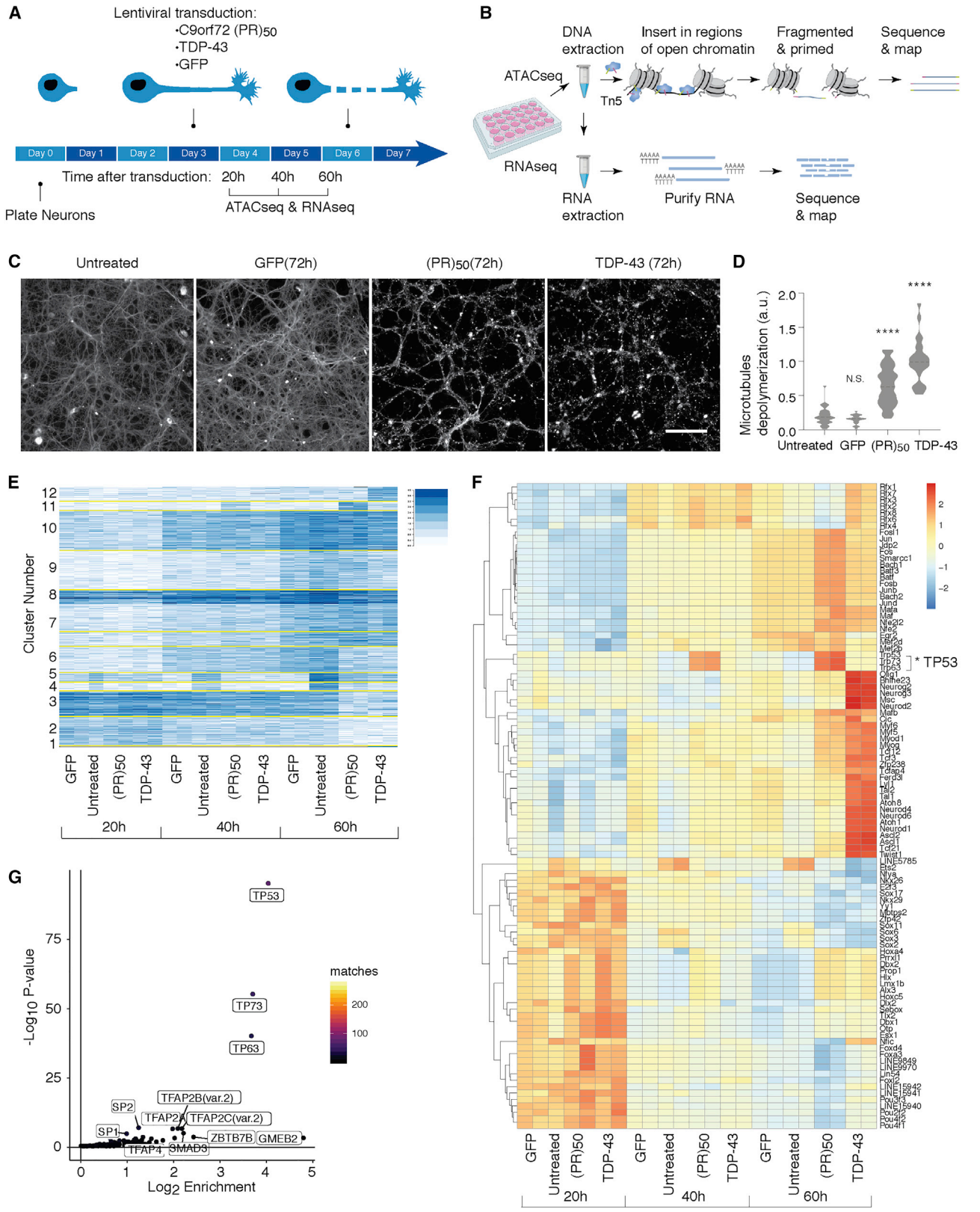

(legend on next page)

Gendron et al., 2014; Lee et al., 2013; Mori et al., 2013a; Sareen et al., 2013) and/or interfere with essential cellular processes (Coyne et al., 2020). Finally, the repeat-containing RNAs can be translated into dipeptide repeat (DPR) proteins (Ash et al., 2013; Gendron et al., 2013; Mori et al., 2013b; Zu et al., 2013). These DPRs include glycine-alanine (GA), glycine-proline (GP), glycine-arginine (GR), proline-arginine (PR), and proline-alanine (PA); they accumulate in the brains of patients with *C9orf72* mutations, and some of them are cytotoxic in cell and animal models (Gitler and Tsuiji, 2016). Notably, the arginine-rich DPRs, GR and PR, are the most toxic ones (Kwon et al., 2014; Mizielinska et al., 2014; Wen et al., 2014), but perplexingly, these two are not as abundant in patient brains as some of the other ones (Davidson et al., 2014; Mackenzie et al., 2015; Saberi et al., 2018; Sakae et al., 2018; Schludi et al., 2015), raising the question of their relevance to pathogenesis. On the other hand, these toxic DPRs could be key contributors to early facets of disease, but because they are so toxic, they would not be present at detectable levels at end stage.

Emerging studies have suggested a role for alterations in epigenetic regulation in ALS and FTD, including DNA methylation, chromatin remodeling, and histone post-translational modification (Barry et al., 2011; Belzil et al., 2016; Berson et al., 2017; Chesi et al., 2013; Cobos et al., 2019; Martin and Wong, 2013). To explore the epigenetic landscape and cellular mechanisms driving neurodegeneration, we sought to define the programs of gene expression and their regulators within neurons in response to pathogenic protein accumulation. Gene expression is regulated by the binding of transcription factors (TFs) to specific DNA sequence motifs across the genome. TFs do not always have access to these binding sites, because the DNA is packaged into chromatin. The accessibility of these sites to TFs is tightly regulated. The assay for transposase-accessible chromatin using sequencing (ATAC-seq) is a high-throughput method that quantifies regions of the genome with open chromatin sites—ones that are accessible to TFs and thus transcriptionally active (Buenrostro et al., 2013, 2015; Corces et al., 2017). This technique has been used to address a wide variety of biological questions, profiling the epigenetic features of chromatin state and DNA accessibility (Greenleaf, 2015). Owing to technical difficulties, ATAC-seq has not yet been applied to primary neurons.

To analyze the epigenomic landscape of neurodegeneration caused by ALS-associated protein aggregation, we developed a modified version of ATAC-seq that works on primary neurons. We discovered that *C9orf72*-ALS/FTD associated poly(PR) activated a remarkably specific signature of chromatin accessibility, involving transcriptional targets of the tumor suppressor gene p53. Our findings reveal an unexpected role of p53 as a mediator of neurodegeneration elicited by poly(PR) and provide an example of how ATAC-seq can now be applied to neurons to define mechanisms of neurodegeneration.

RESULTS

The chromatin accessibility landscape of primary cortical neurons treated with *C9orf72* $(PR)_{50}$ or TDP-43

Two ALS-associated proteins, TDP-43 and poly(PR) dipeptides produced from the *C9orf72* hexanucleotide repeat expansion, form aggregates, and cause degeneration *in vitro* and *in vivo* (Kwon et al., 2014; Neumann et al., 2006; Wen et al., 2014; Zhang et al., 2019). But do they do so by similar or different mechanisms? To obtain a comprehensive and integrative picture of the chromatin and transcriptional landscape of cortical neurons after ALS/FTD-associated protein accumulation, we set up an *in vitro* system where we could monitor neuronal cell death and axonal degeneration elicited by either poly(PR) or TDP-43 accumulation. We cultured embryonic day 16.5 (E16.5) mouse primary cortical neurons for 3 days to allow their processes to grow. We transduced them with lentiviruses expressing a 50-repeat poly(PR) protein, $(PR)_{50}$, transactive response DNA binding protein 43 kDa (TDP-43), or green fluorescent protein (GFP) as a negative control (Figures 1A and S1A–S1J). Both $(PR)_{50}$ and TDP-43 caused marked cell death and axonal degeneration 72 h after transduction. $(PR)_{50}$- and TDP-43-expressing neurons formed numerous tubulin βIII puncta, indicating that microtubules disassembled, and the axons underwent degeneration (Figures 1C and 1D).

Both TDP-43 and $(PR)_{50}$ elicited neurodegeneration that looked grossly similar (Figures 1C and 1D), but we wondered whether the underlying chromatin regulation and gene expression programs driving degeneration were the same or different. ATAC-seq is a high-throughput method that quantifies regions of the genome with open chromatin sites—ones that are accessible to TFs and thus transcriptionally active. To probe chromatin accessibility in primary neurons, we developed a modified version of ATAC-seq. Recent methodological advances in the assay have enabled the generation of high-fidelity chromatin accessibility profiles for a variety of cell types (Corces et al., 2017). However, so far, this assay has not been applied to primary neurons *in vitro*. The dissociation of cultured primary neurons, one of the first steps performed in the standard ATAC-seq protocol (Buenrostro et al., 2013, 2015; Corces et al., 2017), causes neuron death, which interferes with ATAC-seq results

Figure 1. Chromatin accessibility landscape of cortical neurons treated with GFP, *C9orf72* $(PR)_{50}$, or TDP-43

(A) Schematic illustration of the experimental design.

(B) On-plate direct lysis followed by nuclei isolation was used to extract neuronal DNA. Hyperactive Tn5 transposase inserted sequencing adapters into open chromatin regions was used to prepare ATAC-seq libraries. A sequential RNA lysis step was performed after the direct DNA lysis to perform RNA-seq.

(C and D) Cortical primary neurons were cultured for 3 days and either treated with GFP, *C9orf72* $(PR)_{50}$, or TDP-43 for an additional 72 h or left untreated. Axonal microtubules (MTs) were depolymerized and degraded after treatment with $(PR)_{50}$ and TDP-43 (C). Quantification in (D), as described in STAR methods (t test; ****$p < 0.0001$; N.S., not significant). Scale bar, 100 μm.

(E) K-means clustering ($k = 12$) of the top 3,960 variable peaks from the ATAC-seq analysis.

(F) Heatmap showing scaled chromVAR deviation scores across variable genes.

(G) Two-sided Fisher's exact test enrichment p values of cluster 11 TFs from (E) against the background of all other clusters. Cluster 11 shows highest enrichment for p53 TF and its family members (p63 and p73).

and motivated us to optimize the protocol for use with primary neurons (see STAR methods). Briefly, to avoid neuronal cell death as a result of dissociation, we instead used direct lysis of plated neurons, followed by isolation of released nuclei (Figures 1B and S2A–S2C). To probe chromatin accessibility, we harvested neurons 20, 40, and 60 h following transduction of $(PR)_{50}$-, TDP-43-, or GFP-expressing lentiviruses. We chose these time points because they preceded the onset of neuronal morphological changes accompanying cell death and axonal degeneration. We performed sequential DNA and RNA extraction so we could obtain both regions of open chromatin (by ATAC-seq) as well as the transcriptional program of neurons *in vitro* (by RNA sequencing [RNA-seq]) (Figure 1B).

Our ATAC-seq measurements of DNA accessibility displayed a wide array of changes during each treatment over the time course of the experiment. To track the differential DNA accessibility profiles, we used principal-component analysis (PCA) (Figures S2D and S2E). The first principal component (PC1) explains the greatest possible variance in the neuronal data, reflecting the changes in chromatin accessibility that occur in neurons in culture over time. PC2 explains the second greatest proportion of variance, reflecting accessibility changes that occur only at later time points (40 and 60 h) and specifically in neurons expressing TDP-43 or $(PR)_{50}$ (Figures S2D and S2E). The first two PCs are used for visualization, since they capture most of the variation from the dataset. These differential variations reflect the neuronal chromatin accessibility response to $(PR)_{50}$ and TDP-43 over time (Figures S2F–S2L).

To characterize time-dependent modules of accessible chromatin regions, we first determined the most highly variable regions. We found 3,960 different genomic regions that showed high variability both at different time points and under different treatment conditions (Figure 1E). We used k-means clustering (k = 12) to identify different behaviors between the different conditions and time points. The clustering captures strong changes across time between all treatments, including gain of accessibility (clusters 6–10) and loss of accessibility (clusters 1–3). We detected loss of accessibility in TDP-43, $(PR)_{50}$ and GFP treated neurons (compared to untreated neurons), across all time points (clusters 4 and 5). We also detected regions that were more accessible for TDP-43 at 60h (cluster 12) and at 40 and 60 h for $(PR)_{50}$ (cluster 11) (Figure 1E). Thus, applying a modified version of the ATAC-seq protocol adapted for use with primary neurons, we generated diverse regulatory landscapes of neurodegeneration induced by the accumulation of distinct ALS-associated proteins.

In addition to quantitative genome-wide information on chromatin accessibility, ATAC-seq also affords the opportunity to identify predicted TF-binding events located in the open chromatin regions (Schep et al., 2017). In other words, are there any TF sequence motifs enriched in the ATAC-seq peaks? To identify TF binding motifs that are enriched at differentially accessible regions in neurons expressing TDP-43, $(PR)_{50}$, or GFP, we applied chromVAR (Figure 1F). This bioinformatic approach facilitates the analysis of chromatin accessibility data by estimating gain or loss of accessibility within peaks sharing the same motif, while controlling for technical biases (Schep et al., 2017). We clustered the top 100 differential TFs according to their deviation scores. We observed many differences in TF accessibility at 60 h in neurons expressing TDP-43, but remarkably, only a single TF family, the p53 family (comprising p53, p63, and p73), was altered in *C9orf72* $(PR)_{50}$-treated neurons (Figure 1F). Indeed, when we examined predicted p53 family binding across the different clusters of ATAC-seq peaks, the p53, p63, and p73 binding motifs were significantly enriched only in cluster 11, the same cluster that captures the *C9orf72* $(PR)_{50}$ specific changes occurring after 40 and 60 h of treatment (Figure 1E). Furthermore, in cluster 11 p53 was the most enriched TF predicted to bind to the *C9orf72* $(PR)_{50}$ open regions (Figure 1G). Thus, whereas neurodegeneration induced by TDP-43 accumulation seems to involve activation of a diverse set of regulatory elements throughout the genome, mediated by a wide range of TFs, the response to *C9orf72* $(PR)_{50}$ is remarkably specific to regulatory elements enriched in binding sites for a single TF family, p53.

The transcriptional program of primary cortical neurons treated with $(PR)_{50}$ is mediated by p53

The enrichment of predicted p53-binding sites in regions of open chromatin in neurons expressing $(PR)_{50}$ suggests p53 is mediating the neuronal response, but it does not prove it. To provide direct evidence that p53 transcriptional targets are activated (or repressed) in neurons in response to $(PR)_{50}$, we performed RNA-seq on $(PR)_{50}$, TDP-43, and GFP-treated neurons at 20, 40, and 60 h. Visualizing RNA-seq data using PCA (Figures S3A and S3B) reveals that the largest amount of variation reflects neuronal gene changes that occur over time. PC2 reflects changes that occur only at later time points (40 and 60 h), capturing the divergence in neuronal responses to TDP-43 and $(PR)_{50}$ compared with GFP-treated and untreated neurons (Figure S3A). Notably, the variation in gene expression between TDP-43 and $(PR)_{50}$ mirrors the DNA accessibility data, underscoring unique footprints of chromatin accessibility and transcriptional programs in TDP-43- and $(PR)_{50}$-treated neurons.

Analyzing the differentially expressed genes in neurons after 60 h of $(PR)_{50}$ treatment revealed that the most highly upregulated genes were *Cdkn1a*, *Puma* (*Bbc3*), *Trp53inp1*, *Ccng1*, *Sulf2*, and *Fam212b* (Figure 2A). Remarkably, these are all bona fide p53 target genes (Brady and Attardi, 2010). Importantly, the transcription program in the TDP-43-expressing neurons is not clearly associated with p53 (Figure 2B). Furthermore, KEGG (Kyoto Encyclopedia of Genes and Genomes) pathway analysis of 6,103 differentially expressed genes revealed p53 signaling to be the most enriched pathway in the gene sets specifically upregulated after $(PR)_{50}$ treatment (cluster 2; Figures 2C and S3C). Thus, p53 target genes are specifically activated in neurons expressing $(PR)_{50}$, consistent with the DNA accessibility results.

To identify cellular pathways affected by $(PR)_{50}$ and TDP-43 treatment, we utilized weighted gene co-expression network analysis (WGCNA) (Figure S3D). WGCNA is a computational approach for studying biological networks (Langfelder and Horvath, 2008). It can be applied to large, high-dimensional datasets to identify clusters (modules) of highly correlated genes. We identified 17 gene modules, 8 and 9 of which are dysregulated in $(PR)_{50}$ and TDP-43, respectively (Figure S3D). One

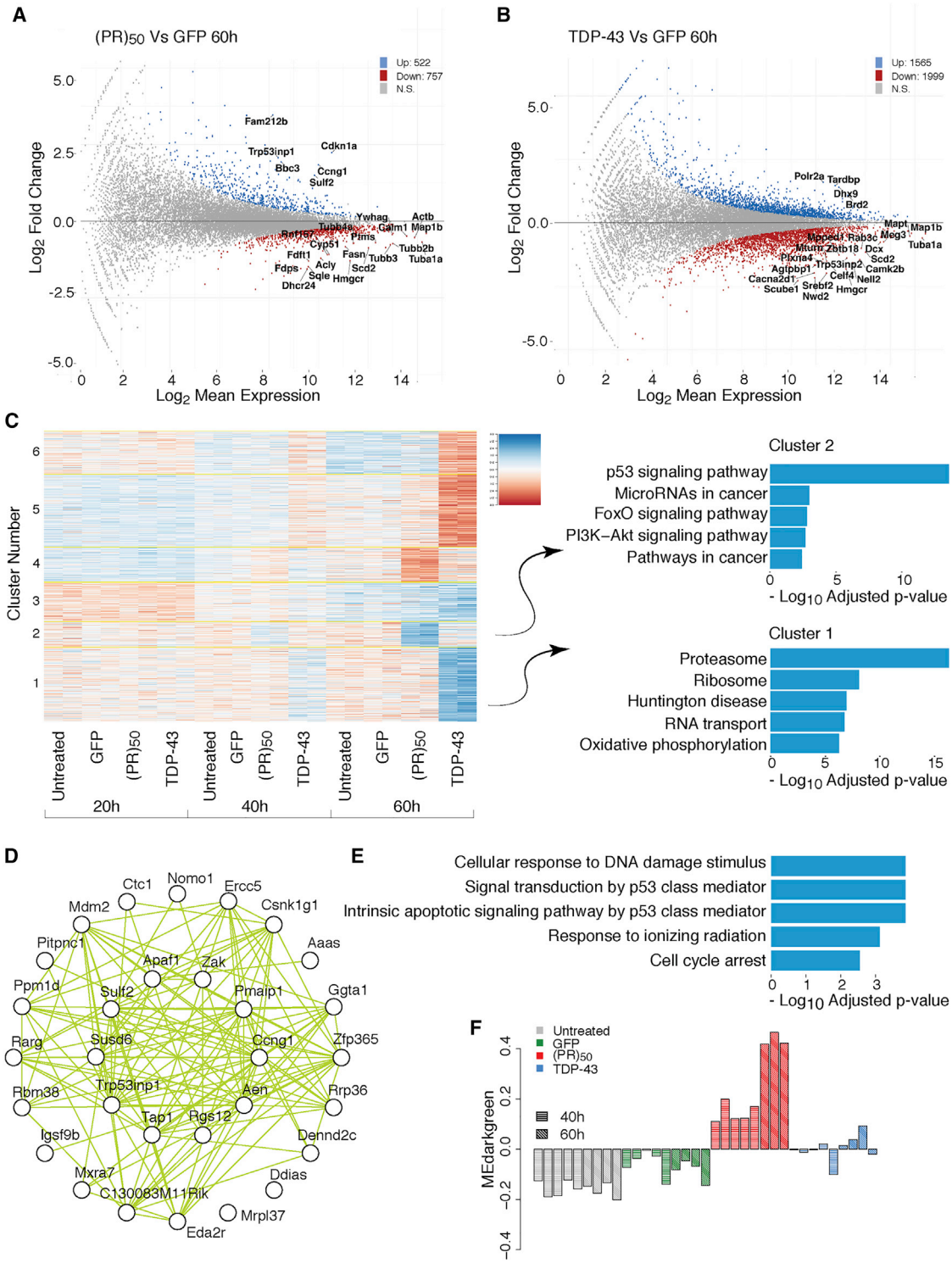

Figure 2. The transcription program of cortical neurons treated with GFP, *C9orf72* $(PR)_{50}$, or TDP-43

(A and B) MA plot 60 h after treatment with $(PR)_{50}$ versus GFP in (A) and TDP-43 versus GFP-treated neurons in (B).

(C) K-means clustering (k = 6) of the top 6,109 variable transcripts. KEGG pathway Gene Ontology enrichment of clusters 1 and 2. FDR corrected p value.

(D–F) Average linkage hierarchical clustering using the topological overlap metric for co-expression dissimilarity. Modules were identified from the dendrogram (presented in Figure S3D) and labeled with colors. (D) Top 30 hub genes and 300 connections for co-expression module darkgreen. (E) Top Gene Ontology enrichments for co-expression module darkgreen. FDR corrected p value. (F) Eigengene values of the darkgreen module for each individual sample.

module of particular interest is the module labeled as dark-green (Figure S3E), which is specifically upregulated in $(PR)_{50}$ (Figures 2F and S3F). This module is highly enriched in genes annotated with p53 related functions, including cellular response to DNA damage, cell cycle arrest and intrinsic apoptotic signaling (Figure 2E), as well as direct targets of p53 (Figure 2D), supporting the findings from the differential expression analysis. These changes in cellular pathways and gene expression, together with the chromatin accessibility findings point to p53 as potentially a central regulator of the program of neurodegeneration elicited by *C9orf72* $(PR)_{50}$.

p53 is stabilized in neurons in response to *C9orf72* $(PR)_{50}$

Under normal conditions p53 is present in cells at very low levels (Boehme and Blattner, 2009; Meek and Anderson, 2009; Soussi, 2000). In response to a variety of cellular stressors, including DNA damage, p53 becomes rapidly stabilized and activated (Fielder et al., 2017). Once activated p53 helps cells to mount a response to the cellular damage by both transcription-dependent and independent mechanisms (Culmsee and Mattson, 2005; Kastenhuber and Lowe, 2017). We performed immunoblotting of lysates of neurons treated with $(PR)_{50}$, TDP-43, or GFP (Figures 3A and 3B), using a p53-specific antibody (Figure S4A). Whereas p53 levels remained barely detectable in neurons expressing GFP or TDP-43, they were significantly elevated 72 h after $(PR)_{50}$ induction (Figures 3A and 3B).

To further investigate whether p53 elevated levels are due to protein stabilization or as a result of its transcriptional and/or translational upregulation, we performed chase experiments with the protein synthesis inhibitor cycloheximide. We treated neurons with cycloheximide after 48 h of $(PR)_{50}$ expression, a time point at which p53 RNA levels did not change (Figures S4B–S4D). Following 24 h of cycloheximide treatment, we lysed neurons and analyzed p53 protein levels by immunoblotting (Figure S4B–S4D). p53 protein levels increased following $(PR)_{50}$ treatment, even in the presence of cycloheximide, indicating p53 protein stabilization instead of increased synthesis. Together, these data provide evidence that p53 is specifically stabilized in neurons in response to *C9orf72* $(PR)_{50}$.

p53 ablation protects neurons from axonal degeneration and cell death caused by *C9orf72* $(PR)_{50}$

Having established that *C9orf72* $(PR)_{50}$ expression in neurons stabilizes p53, activates regulatory elements throughout the genome that are enriched for p53-binding sites, and results in the upregulation of key p53 target genes, we next sought to directly test if p53 is required for neurodegeneration induced by *C9orf72* $(PR)_{50}$. We cultured primary cortical neurons from p53 knockout (KO) mice and from their wild-type (WT) littermates for 3 days and transduced them with lentiviruses expressing TDP-43 or $(PR)_{50}$. Strikingly, p53 KO neurons were completely protected from degeneration caused by $(PR)_{50}$ (Figures 3C and 3D). This level of protection from degeneration conferred by p53 ablation was long-lasting, and p53 KO neurons survived and did not show any sign of cell death or axonal degeneration for over 7 days. Importantly, p53 KO neurons were not simply resistant to cell death, because expression of TDP-43 caused visible microtubule disassembly and axonal degeneration (Figure 3E-3F).

We next asked whether p53 is required for neurodegeneration induced by a different DPR, poly(glycine-arginine); GR. The arginine-rich DPRs, PR and GR, are the most toxic ones translated from the *C9orf72* repeat expansion (Kwon et al., 2014; Mizielinska et al., 2014; Wen et al., 2014), and pathological evidence suggests GR accumulation correlates well with neurodegeneration in C9ALS/FTD (Sakae et al., 2018). Notably, GR is translated from the sense-strand GGGGCC repeat, whereas PR is produced from the antisense strand (GGCCCC) (Zu et al., 2013). We cultured primary cortical neurons for 3 days and transduced them with lentiviruses expressing $(GR)_{50}$ (Figures 3G–3L). We found elevated levels of GR in neurons by immunoblotting at 120 h of $(GR)_{50}$ expression (Figures 3G and 3H). By 168 h, we detected elevated p53 levels in neurons expressing $(GR)_{50}$ (Figures 3I and 3J) and the initiation of microtubule disassembly and axonal degeneration in WT neurons. These effects were strongly attenuated in p53 KO neurons (Figures 3K and 3L). Thus, similar to its protective effects on $(PR)_{50}$ toxicity, p53 ablation suppresses axonal degeneration induced by $(GR)_{50}$.

In addition to axonal degeneration, we also tested p53's role in neuronal cell death. Caspases are cellular mediators of programmed cell death that exist in an inactive precursor state and are activated by proteolytic cleavage (Hengartner, 2000). One of these, caspase-3, is an initiator of the cell death cascade and thus a marker of a cell's initiation of cell death. We cultured primary cortical neurons from p53 KO mice and their WT littermates for 3 days and transduced them with lentiviruses expressing $(PR)_{50}$ (Figures 4A–4D). We detected elevated levels of cleaved caspase-3 in WT neurons by immunoblotting after 72 and 96 h of $(PR)_{50}$ expression (Figures 4A–4D). Importantly, cleaved caspase-3 was undetectable, across all time points, in p53 KO neurons, providing evidence that p53 KO neurons are completely protected from $(PR)_{50}$-induced neurodegeneration (Figures 4A–4D). The difference in cell death and axonal degeneration in p53 KO neurons was not a result of reduced levels of $(PR)_{50}$ expression, because $(PR)_{50}$ levels in neurons from both p53 KO and their WT littermates were similar at 72 h (Figures 4G and 4H). Interestingly, at later time points, we were only able to detect $(PR)_{50}$ in p53 KO neurons, owing to the fact that nearly all of the WT neurons expressing $(PR)_{50}$ had undergone degeneration by 96 h (Figures 4J and 4K). Thus, p53 KO neurons are able to completely resist the toxicity of *C9orf72* $(PR)_{50}$ accumulation.

DNA fragmentation is a hallmark of apoptosis that is induced by apoptotic stimuli and mediated by the family of caspases. Apoptotic DNA fragmentation induces phosphorylation of H2AX on Ser139. Phosphorylation of H2AX to produce γH2AX is a key event in the repair of DNA damage and the induction of DNA degradation leading to cell death (Kitazumi and Tsukahara, 2011; Rogakou et al., 2000). Consistent with previous findings where ectopic expression of poly(GR) increased γH2AX, the marker of DNA damage (Lopez-Gonzalez et al., 2016), we also detected elevated levels of γH2AX in WT neurons upon $(PR)_{50}$ treatment. Strikingly, γH2AX induction was markedly reduced in p53 KO neurons (Figures 4E–4G, 4I, 4J, and 4L). Beyond *C9orf72,* DNA damage and defects in DNA damage repair in

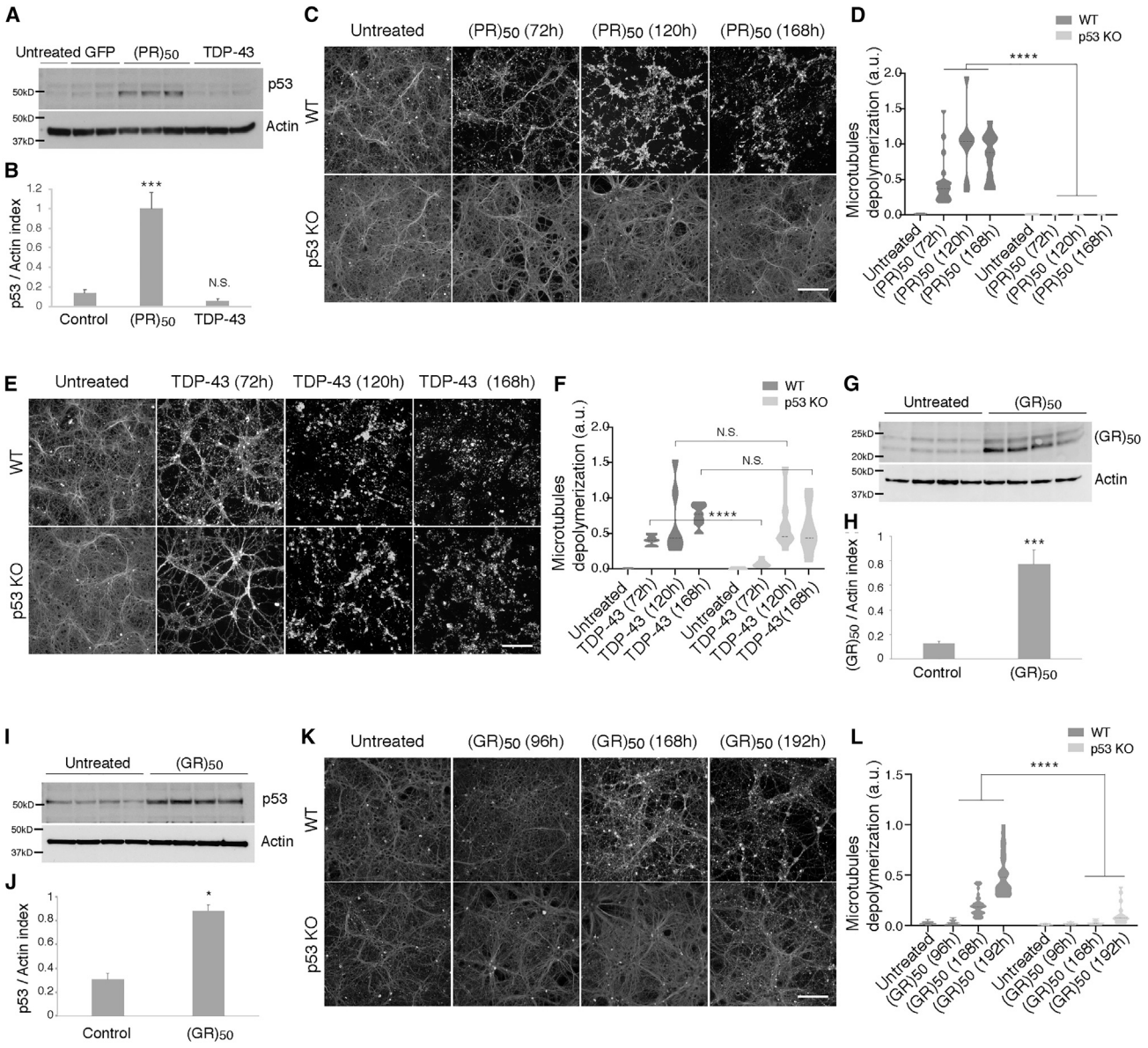

Figure 3. p53 ablation protects neurons from axonal degeneration elicited by *C9orf72* DPRs

(A and B) p53 levels were elevated in $(PR)_{50}$-treated neurons (A). Quantification of p53 levels by immunoblotting and normalized to actin (B). Graphs show mean ± SEM (t test; ***p < 0.001; N.S., not significant).

(C–F). Axonal microtubules (MTs) of WT cortical neurons were depolymerized and degraded after treatment with $(PR)_{50}$ or TDP-43. The p53 KO cortical neurons and axons were completely protected from any degradation after $(PR)_{50}$ treatment (C), but not after TDP-43 treatment (E). Quantification shown in (D) and (F), as described in STAR methods (t test; ****p < 0.0001; N.S., not significant). Scale bar, 100 μm.

(G–J) WT cortical neurons treated with $(GR)_{50}$ resulted in $(GR)_{50}$ caused enhanced levels of p53 (I and J). Quantitation of $(GR)_{50}$ and p53 was determined by immunoblots and normalized to actin (H and J). Graphs show mean ± SEM (t test; *p < 0.05, ***p < 0.001; N.S., not significant).

(K and L) Cortical neurons from p53 KO embryos or their WT littermates were either left untreated or treated with C9orf72 $(GR)_{50}$. (K) Degeneration induced by $(GR)_{50}$ was attenuated in p53 KO cortical neurons and quantified in (L), as described in STAR methods (t test; ****p < 0.001). Scale bar, 100 μm.

neurons have been previously implicated in ALS caused by mutations in FUS (Qiu et al., 2014; Wang et al., 2013).

To carefully monitor axonal and cell death we used live-cell imaging, coupling the power of time-lapse video microscopy, high-definition phase-contrast imaging with automated image processing algorithms tailored here to analyze axonal state and neuronal fate. WT neurons exhibited fragmented axons and smaller diameter soma, reflecting axonal degeneration and cell death following expression of $(PR)_{50}$ (Figures S4E and S4F). In contrast, p53 KO neurons and axons had no reduction in size or fragmentation after $(PR)_{50}$ expression (Figures S4E and S4F). p53 KO neurons and axons degenerated

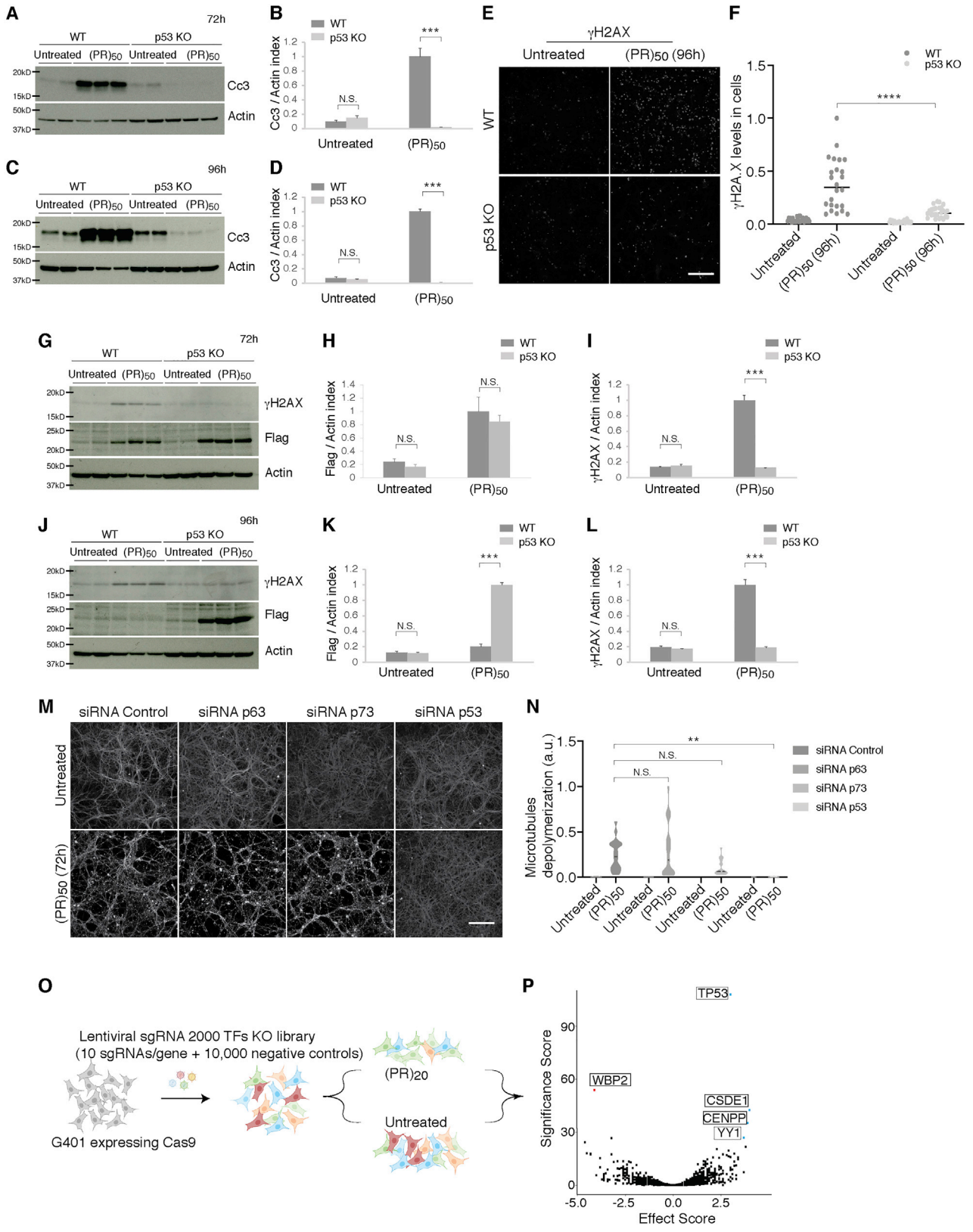

(legend on next page)

upon TDP-43 expression (Figures S4G and S4H). Taken together, our results show that p53 KO neurons and their axons are completely protected from the toxic effects of $(PR)_{50}$, but not from TDP-43.

In addition to p53, our chromatin accessibility profiling data also highlighted p63 and p73, since they share similar binding motifs to p53 (Figures 1F and 1G). To test their role in axonal degeneration and cell death in response to $(PR)_{50}$, we treated primary cortical neurons with p53, p63, p73, or nontargeting small interfering RNA (siRNA) for 48 h before the addition of $(PR)_{50}$. Whereas p53 knockdown conferred complete protection against axonal degeneration and cell death, p63 or p73 knockdown did not (Figures 4M and 4N). Thus, p53 seems to be the key TF mediating $(PR)_{50}$ toxicity in this system. Interestingly, in a related study, p53 (but not p63 or p73) is shown to play a central role in axonal degeneration during the development of the peripheral nervous system in dorsal root ganglia (DRG) following trophic deprivation (M.T.-L. and D.J.S., unpublished data).

Next, we asked whether p53 reduction can prevent axonal degeneration after $(PR)_{50}$ is already expressed and the degeneration cascade begins. Reducing p53 levels using siRNA within the first 24 h of $(PR)_{50}$ expression is protective, and no axonal degeneration can be detected (Figures S5A and S5B). If we add the p53 siRNA after 24 h, it is not as protective as when added at earlier time points (Figure S5A and S5B). To test whether p53's role in degeneration caused by $(PR)_{50}$ is driven primarily by cell-autonomous effects within neurons or instead by the non-neuronal cells (e.g., the glia present in the primary cultures), we treated neuronal cultures with FUdR (5-fluoro-2′-deoxyuridine). This drug interferes with DNA synthesis and inhibits cell division, resulting in depletion of glia from the culture, as detected by GFAP immunostaining (Figure S5C). Even in the absence of glia, the p53 KO neurons were protected from $(PR)_{50}$-induced degeneration (Figures S5D and S5E). Thus, p53 functions within neurons to mediate degeneration.

In a recent genome-wide CRISPR-Cas9 screen for modifiers of *C9orf72* DPR toxicity modifiers, we did not identify p53 (Kramer et al., 2018). For that screen, we used the human chronic myelogenous leukemia (CML) K562 cell line. This cell line harbors a p53 mutation (Law et al., 1993), and these cells have likely developed p53-independent cell death mechanisms. We therefore repeated the screen in a WT p53 expressing human cell line, using the kidney rhabdoid tumor G401 cell line (Idelman et al., 2003), screening a single-guide RNA (sgRNA) library targeting ~2,000 TFs. Remarkably, in this G401 cell line, we found p53 KO as the strongest suppressor of $(PR)_{50}$ toxicity (Figures 4O and 4P). These results further underscore a central role of p53 in mediating cell death elicited by $(PR)_{50}$.

p53 ablation extends lifespan in a mouse model of C9orf72 $(PR)_{50}$

Given the striking resistance of p53 KO neurons to $(PR)_{50}$ toxicity *in vitro*, we next asked whether p53 ablation could also confer this protection *in vivo*. We used an adeno-associated virus (AAV)-vector-based transgenic mouse model engineered to express *C9orf72* poly(PR) throughout the brain. These mice develop neuron loss, gliosis, behavioral impairments, and early lethality (Zhang et al., 2019). We delivered an AAV vector expressing GFP-tagged $(PR)_{50}$ via intracerebroventricular administration at post-natal day 0 (P0) (Figure 5A). Consistent with the reported toxicity of $(PR)_{50}$ in this model (Zhang et al., 2019), 95% of WT GFP-$(PR)_{50}$-expressing mice died by day 39 (Figures 5B and S6A). KO of p53 significantly improved lifespan (log-rank test for trend, $p = 0.0116$; hazard ratio [HR], 2.34), resulting in a 2.5-fold improvement in median lifespan, with several mice surviving more than 150 days (Figures 5B and S6A). Notably, p53 KO mice are highly predisposed to malignancy, reflected in a greatly accelerated rate of tumorigenesis compared with heterozygous (Het) or WT mice (Jacks et al., 1994). By 3 months, they started developing tumors, and by 6 months, almost all KO mice had died (Jacks et al., 1994). Consistent with these findings, the p53 KO mice expressing $(PR)_{50}$ had died or had to be sacrificed beginning at 3 months of age, as obvious tumors were detected (Figures 5B and S6B). This suggests that the 2.5-fold improvement in lifespan might actually be an underestimate of the ability of p53 KO to protect against $(PR)_{50}$-induced early lethality. Even Het reduction of p53 conferred partial rescue of GFP-$(PR)_{50}$ toxicity (Figure 5B). Thus, genetic reduction of p53 is sufficient to extend survival in an aggressive mouse model of neurodegeneration caused by *C9orf72* $(PR)_{50}$.

To test whether reducing p53 levels can rescue neurodegenerative phenotypes caused by TDP-43 accumulation *in vivo*, we used a genetic approach. We choose a mouse line expressing human WT TDP-43 that displays a rapidly progressing phenotype (Wils et al., 2010). Homozygous mice harboring two copies of this TDP-43 transgene display profound motor

Figure 4. p53 ablation rescues neurons from DNA damage, cell death, and axonal degeneration elicited by *C9orf72* $(PR)_{50}$

(A–D) WT neurons treated with $(PR)_{50}$ resulted in enhanced activation (cleavage) of caspase-3, as evaluated by immunoblot analysis. Genetic ablation of p53 inhibited this activation of caspase-3. Quantitation of cleaved caspase-3 was determined by immunoblots and normalized to actin (B and D). Graphs show mean ± SEM (t test; ***$p < 0.001$; N.S., not significant).

(E–L) Phosphorylated H2AX (γH2AX) levels were elevated after $(PR)_{50}$ treatment, and p53 ablation inhibited this induction at 72 h (G and I) and 96 h (E, F, J, and L). Quantitation of γH2Ax following $(PR)_{50}$ treatment was determined by immunoblotting and normalized to actin (I and L) and by immunostaining normalized to the number of cells (F). Graphs show mean ± SEM (t test; ***$p < 0.001$, ****$p < 0.0001$; N.S., not significant). (G and H) $(PR)_{50}$ levels were elevated at 72 h in both WT and p53 KO of $(PR)_{50}$-treated neurons. At 96 h, $(PR)_{50}$ was present only at p53 KO and not at WT neurons (J and K), as detected using the anti-FLAG antibody. (M and N) WT cortical neurons treated with siRNA against *p53*, *p63*, or *p73*, or nontargeting control siRNA treated with $(PR)_{50}$. Axonal microtubules (MTs) were depolymerized and degraded after $(PR)_{50}$ in nontarget control, *p63*, and *p73*, yet *p53* reduction by siRNA delayed $(PR)_{50}$ axonal degeneration (M). Quantification shown in (N), as described in STAR methods (one-way ANOVA; **$p < 0.01$; N.S., not significant). Scale bar, 100 μm.

(O and P) Schematic illustration of pooled CRISPR-Cas9 screening paradigm. G401 cells expressing Cas9 were transduced with a lentiviral sgRNA library (10 sgRNAs per gene) and treated with $(PR)_{20}$. Volcano plot for genes in the $(PR)_{20}$ screen (P). Blue indicates all genes conferring resistance to $(PR)_{20}$ when knocked out (1% false discovery rate [FDR]), and red indicates all genes conferring sensitivity to $(PR)_{20}$ when knocked out (1% FDR). p53 was the top hit conferring resistance to $(PR)_{20}$.

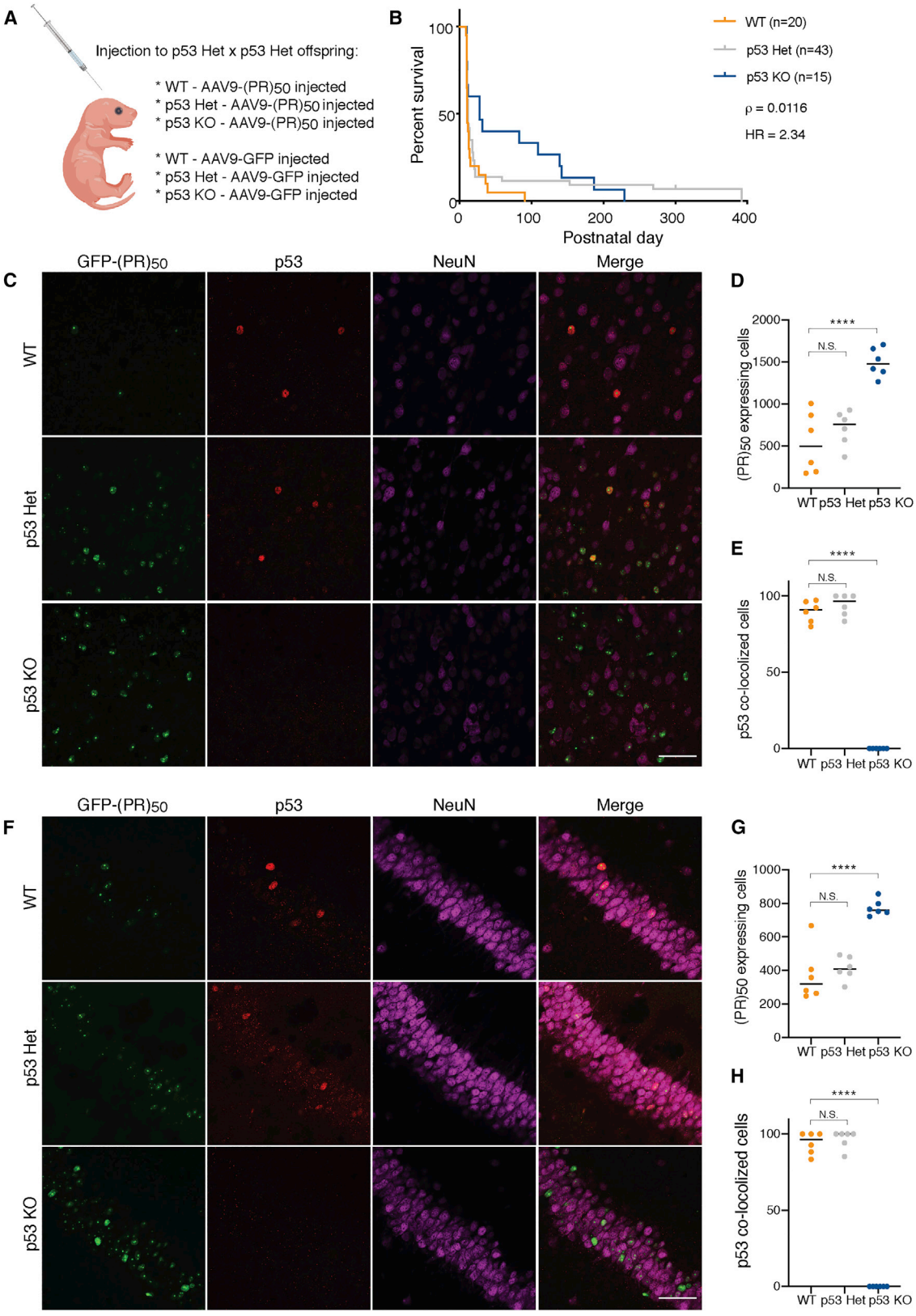

(legend on next page)

dysfunction, resulting in an inability to walk at ~P21 and death at ~P24 (Wils et al., 2010). We crossed TDP-43 hemizygous mice with p53 Het mice to produce TDP-43 hemizygous with p53 Het offspring and then intercrossed these mice to produce TDP-43 homozygous p53 KO, Het, or WT littermates. Decreased levels of p53 in TDP-43 homozygous transgenic mice did not improve their lifespan, nor did the complete removal of p53 (log-rank test for trend, p = 0.95; HR, 1.03; Figure S6C). Thus, like the *in vitro* results, p53 KO does not protect against TDP-43 *in vivo* in this transgenic mouse. We note that a previous study observed protection from mutant TDP-43-induced death of neural progenitors in p53 KO embryos compared to WT embryos and in human induced pluripotent stem cell (iPSC)-derived cortical neurons (Vogt et al., 2018). It will be interesting to compare and contrast cell death pathways that are active in the embryo and adult and the role of p53 in activating these pathways in response to TDP-43.

To investigate p53 levels in the *C9orf72* $(PR)_{50}$ mouse model *in vivo*, we used immunostaining with a p53-specific antibody (Figures 5C, 5F, S4A, and S6D–S6H). We detected strong induction of p53 in neurons in the cortex and hippocampus of GFP-$(PR)_{50}$-expressing WT mice at 3 weeks (Figures 5C, 5D, 5F, 5G, and S6F–S6H). In contrast, we did not detect p53 in p53 KO mice (which perforce eliminates p53 expression) expressing GFP-$(PR)_{50}$ or in WT mice expressing GFP (Figures 5C, 5D, 5F, 5G, and S6F–S6H). p53 was almost exclusively colocalized with GFP-$(PR)_{50}$ in neurons of both hippocampus and cortex (94% and 90%, respectively) (Figures 5C, 5E, 5F, 5H, and S6H). Consistent with our *in vitro* findings (Figures 4J and 4K), we observed a marked increase in the number of cells expressing $(PR)_{50}$ in the cortex and hippocampus in p53 KO compared to WT mice (Figures 5C, 5D, 5F, 5G, and S6D–S6H). Thus, $(PR)_{50}$ is able to accumulate to high levels in the brain of p53 KO mice because they are resistant to its toxicity. These results may help explain why in human postmortem samples levels of poly(PR) are scarce (Davidson et al., 2014; Mackenzie et al., 2015; Schludi et al., 2015); it appears it is so highly toxic that it cannot accumulate to high levels unless its toxicity is blocked (e.g., by p53 inhibition).

p53 reduction rescues degeneration caused by the *C9orf72* GGGGCC repeat expansion

The *C9orf72* GGGGCC repeat expansion could cause disease by multiple mechanisms beyond just poly(PR) and poly(GR). For example, the other DPRs produced from the repeat by RAN translation (poly(GA), poly(GP), and poly(PA)), as well as the sense (GGGGCC) and antisense (GGCCCC) RNAs themselves, could also be culprits (Gitler and Tsuiji, 2016; Kim et al., 2020). To test if p53 ablation could rescue phenotypes from expression of the expanded GGGGCC repeat itself, we first used a *Drosophila* model of C9-ALS/FTD (Xu et al., 2013; Zhang et al., 2015). We used the UAS/GAL4 system to direct expression of 30 GGGGCC repeats to the *Drosophila* eye (Figure 6A). Upregulation of 30 GGGGCC repeats in the *Drosophila* eye causes age-dependent photoreceptor degeneration, leading to an easily visible "rough" eye phenotype (Figure 6A; Xu et al., 2013). We used three different RNAi lines to knockdown *Drosophila* p53. These RNAi lines have been previously characterized (Ni et al., 2011; Periz et al., 2015; Zhaunova et al., 2016) and demonstrated to reduce p53 protein levels (Periz et al., 2015). All three of these RNAi lines significantly suppressed the rough eye phenotype (Figures 6A and 6B). These data provide evidence that p53 reduction is also able to mitigate phenotypes from the GGGGCC repeat expansion itself.

To investigate if p53 is involved in the pathogenesis of the *C9orf72* GGGGCC repeat expansion in a human model, we used iPSC derived from *C9orf72* ALS patients. DNA damage is increased in motor neurons differentiated from iPSCs of *C9orf72* ALS patients (Lopez-Gonzalez et al., 2016). To determine whether the observed increase in DNA damage is p53 dependent, we analyzed the extent of DNA strand breaks by comet assay (Figures 6C–6G). We used two independent *C9orf72* iPSC lines and their respective isogenic controls, where the repeats were excised by CRISPR-Cas9 editing (Figures 6C and 6D). Partial reduction of p53 (Figures S7A, S7B, 6C, and 6D), using shRNA, decreased DNA damage in *C9orf72* iPSC-derived motor neurons, as indicated by the reduction in the relative tail length and the percentage of DNA in the tail (Figures 6E–6G). We performed immunoblotting of lysates from the two independent *C9orf72* iPSC-derived neurons and their isogenic controls. p53 is phosphorylated on serine 15 and activated in *C9orf72* iPSC-derived neurons (Figures 6H–6J), and the apoptotic marker cleaved caspase-3 is induced. Lowering p53 levels using shRNA was sufficient to decrease the accumulation of phosphorylated p53 and cleaved caspase-3 levels (Figures 6H–6J). Taken together, p53 is activated in *C9orf72* iPSC-derived neurons, inducing DNA damage and the apoptotic machinery.

Finally, we tested the impact of lowering p53 levels on survival phenotypes in motor neurons induced from iPSCs from ALS patients with C9orf72 GGGGCC expansions (iMNs) (Shi et al., 2018). As reported previously, in this *in vitro* culture system, even in the presence of trophic factors, both control and c9ALS iMNs exhibit decreased survival over time in culture (Shi et al., 2018). However, the c9ALS patient iMNs died more rapidly than the control iMNs (Shi et al., 2018; Yamada et al., 2019)

Figure 5. p53 ablation extends lifespan in C9orf72 $(PR)_{50}$ mice

(A and B) Schematic illustration of the experimental design. Newborn pups from p53 heterozygous (Het) × Het crosses were injected intracerebroventricularly (ICV) with AAV encoding GFP-$(PR)_{50}$ or GFP (A). Kaplan-Meier survival curves comparing survival of WT (n = 20), p53 Het (n = 43), and p53 KO (n = 15) GFP-$(PR)_{50}$-expressing mice (B). p53 KO GFP-$(PR)_{50}$-expressing mice showed a 2.5-fold improvement in lifespan compared to WT mice. Curves were compared by log-rank test, and effect size was estimated by a Cox proportional hazards model (HR).

(C–H) Immunofluorescence staining of WT, p53 Het, and KO 3-week-old mice shows p53 activation and colocalization with GFP-$(PR)_{50}$ in the cortex (C–E) and hippocampus (F–H) of WT mice. Three mice per genotype and condition were quantified as described in STAR methods, from a 10× magnification (representative pictures in Figure S6H). The values for p53 colocalization (E and H) and $(PR)_{50}$-expressing cell numbers (D and G) for individual brain hemisphere sections are plotted (one-way ANOVA; ****p < 0.0001; N.S., not significant). Scale bars, 50 μm.

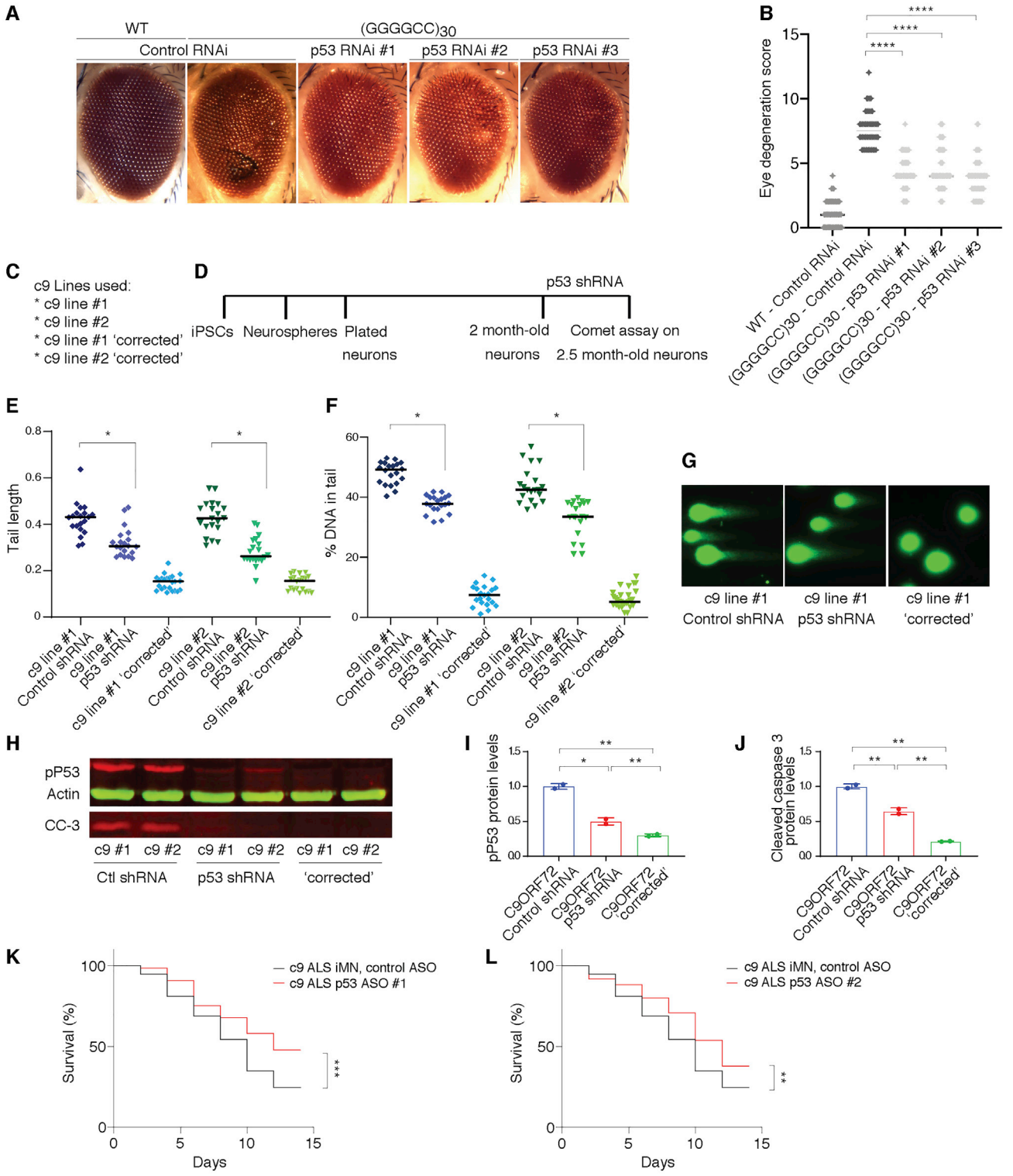

Figure 6. p53 reduction modifies neurodegeneration in C9-ALS models

(A) Representative images of 15-day-old fly eyes expressing 30 GGGGCC repeats (using GMR-GAL4) with RNAi to knock down p53, genetically knocking down three RNAi lines (line 1, P{TRiP.GL01032}attP2; line 2, P{TRiP.GL01220}attP40; and line 3, P{TRiP.HMS02286}attP2). Eye degeneration is quantified in (B). All data are presented as mean ± SD. n = 50 (one-way ANOVA; ****p < 0.0001; N.S., not significant).

(legend continued on next page)

(Figure S7D). We tested two independent antisense oligonucleotides (ASOs) that targeted p53 and one nontargeting control ASO (Figure S7C). Both p53 ASOs markedly increased the proportion of surviving iMNs in the c9ALS lines (Figures 6K and 6L) but did not increase survival of control iMNs (Figures S7E and S7F). These results provide further evidence for a role of p53 in pathologies associated with the *C9orf72* GGGGCC repeat expansion. We note that the protection by lowering p53 in the iPSC-derived motor neurons is not complete, like it was for the p53 KO in the primary mouse neurons treated with poly(PR), suggesting that other disease-causing mechanisms might also contribute to decreased survival in these c9ALS iMNs, such as loss of *C9orf72* function (Shi et al., 2018) and/or contributions from potentially toxic RNA repeats (Coyne et al., 2020).

Puma is a downstream p53 transcriptional target that mediates axonal degeneration and cell death induced by *C9orf72* $(PR)_{50}$

Having established that p53 is activated by expression of *C9orf72* DPRs $(PR)_{50}$ and $(GR)_{50}$ and that this leads to the activation of a p53-dependent transcriptional program culminating in neurodegeneration, we next investigated the downstream mechanism by which p53 mediates $(PR)_{50}$ toxicity. We hypothesized that in response to poly(PR) accumulation, p53 target genes mediating axonal degeneration and cell death would be upregulated. In the mouse primary neuron model, after 40 h of $(PR)_{50}$ expression, p53 upregulated modulator of apoptosis (*Puma*) was the second most upregulated gene after cyclin-dependent kinase inhibitor 1A (*Cdkn1a*) (Figure 7A). Both *Puma* and *Cdkn1a* are known to be tightly regulated by p53 (el-Deiry et al., 1993; Han et al., 2001; Nakano and Vousden, 2001; Yu et al., 2001). Consistent with the elevated transcription levels, we identified an enrichment in ATAC-seq peaks, representing open chromatin regions, near the *Puma* transcriptional start site (Figure 7B), which correspond to the p53-binding sites. Based on these *Puma* chromatin accessibility data and increased *Puma* mRNA levels, together with the fact that *Puma* is a key player in axonal elimination during development of the peripheral nervous system (Maor-Nof et al., 2016; Simon et al., 2016) and that it has a broad role mediating p53-induced cell death (Han et al., 2001; Nakano and Vousden, 2001; Yu et al., 2001), we hypothesized that *Puma* may play a central role in mediating p53's response to *C9orf72* $(PR)_{50}$.

To test a role of *Puma* in axonal degeneration and cell death in response to *C9orf72* $(PR)_{50}$, we treated primary cortical neurons with either *Puma* or nontargeting siRNA for 48 h before the addition of $(PR)_{50}$. Decreased levels of *Puma* significantly delayed axonal degeneration (Figures 7C–7E). Complete removal of *Puma*, using cortical neurons cultured from *Puma* KO mice, conferred even greater protection (Figures 7F–7M). *Puma* ablation attenuated neuronal cell death, as measured by the apoptotic marker cleaved caspase-3 (Figures 7F–7I). Further, *Puma* ablation prevented the induction of γH2AX caused by $(PR)_{50}$ expression (Figures 7J–7M). Finally, *Puma* KO neurons were preserved from axonal fragmentation even after 120 h of $(PR)_{50}$ expression, as detected by live-cell imaging (Figures S4I and S4J). Together, these data provide evidence that *Puma* is at least one of the key downstream p53 targets involved in axonal degeneration and cell death induced by *C9orf72* $(PR)_{50}$.

DISCUSSION

How does *C9orf72* $(PR)_{50}$ lead to p53 activation? One way that poly(PR) accumulation might cause p53 activation in neurons is by eliciting DNA damage. We observe DNA damage in $(PR)_{50}$-treated neurons, but curiously, it seems to be downstream of p53 (Figures 4E–4G, 4I, 4J, and 4L) and *Puma* (Figures 7J–7M) instead of upstream. We also show that DNA damage in motor neurons differentiated from iPSCs of C9orf72 ALS patients is mediated by p53 (Figures 6E–6G). $(PR)_{50}$ activates p53 leading to *Puma* upregulation. Puma has been previously shown to localize to mitochondria, where it induces cytochrome *c* release, leading to a cascade of cleaved caspases and endonuclease activation resulting in DNA fragmentation. Another potential mechanism by which poly(PR) accumulation could activate p53 is via nucleolar stress, a known trigger of p53 activation (Deisenroth et al., 2016; Yang et al., 2018). It has been shown that poly(PR) can cause defects in the nucleolus (Kwon et al., 2014; Tao et al., 2015; Wen et al., 2014; White et al., 2019). Future studies will be aimed at defining the key upstream triggers of p53 activation elicited by *C9orf72* mutations.

p53 was discovered 40 years ago, it is one of the most extensively studied genes (Levine and Oren, 2009), and it has previously been implicated in neurodegeneration. A significant increase in p53 levels and activity was detected in postmortem CNS tissues of patients with ALS as well as in other neurodegenerative diseases, including Alzheimer disease, Parkinson disease, and Huntington disease (Bae et al., 2005; de la Monte et al., 1997; Kitamura et al., 1997; Szybińska and Leśniak, 2017). In ALS, elevated levels of p53 were found in the motor cortex and spinal ventral horn (de la Monte et al., 1998). This increase occurs in regions that are selectively vulnerable to the disease and harbor motor neurons (Martin, 2000). In ALS, expression of mutant SOD1 protein (G93A) or *C9orf72* repeat expansions induces DNA damage and triggers the apoptotic response by activating p53 (Barbosa et al., 2010; Farg et al.,

(C–G) Comet assay analysis after p53 knockdown in iPSC-derived motor neurons from *C9orf72* mutation carriers. (C) The iPSC-derived motor neuron lines used here were differentiated from two independent *C9orf72* mutation carriers and their respective isogenic controls (c9 "corrected"), where repeats were deleted by CRISPR-Cas9. (D) Schematic diagram of the motor neuron differentiation and the shRNA lentivirus transduction. Representative images of the comet assay (G) and quantification of comet length tail (E) and percentage of DNA in the tail (E) in 2.5-month motor neuron cultures (D) from two independent C9ORF72 lines and their respective isogenic controls (t test; *$p < 0.01$).

(H–J) p53 shRNA lentiviral transduction decreases phosphorylated p53 and cleaved caspase-3 levels in iPSC-derived neurons differentiated from two independent *C9orf72* mutation carriers. Quantification of phosphorylated p53 (I) and cleaved caspase-3 (J) levels following p53 shRNA treatments was determined by immunoblotting and normalized to actin. Graphs show mean ± SEM (t test; *$p < 0.05$, **$p < 0.01$).

(K and L) Knockdown of p53 with ASOs extends survival of C9ORF72 ALS (c9 ALS) iMNs (log-rank Mantel-Cox test; n = 3 independent iMN lines with n = 195 iMNs per condition per treatment; **$p < 0.01$,***$p < 0.001$).

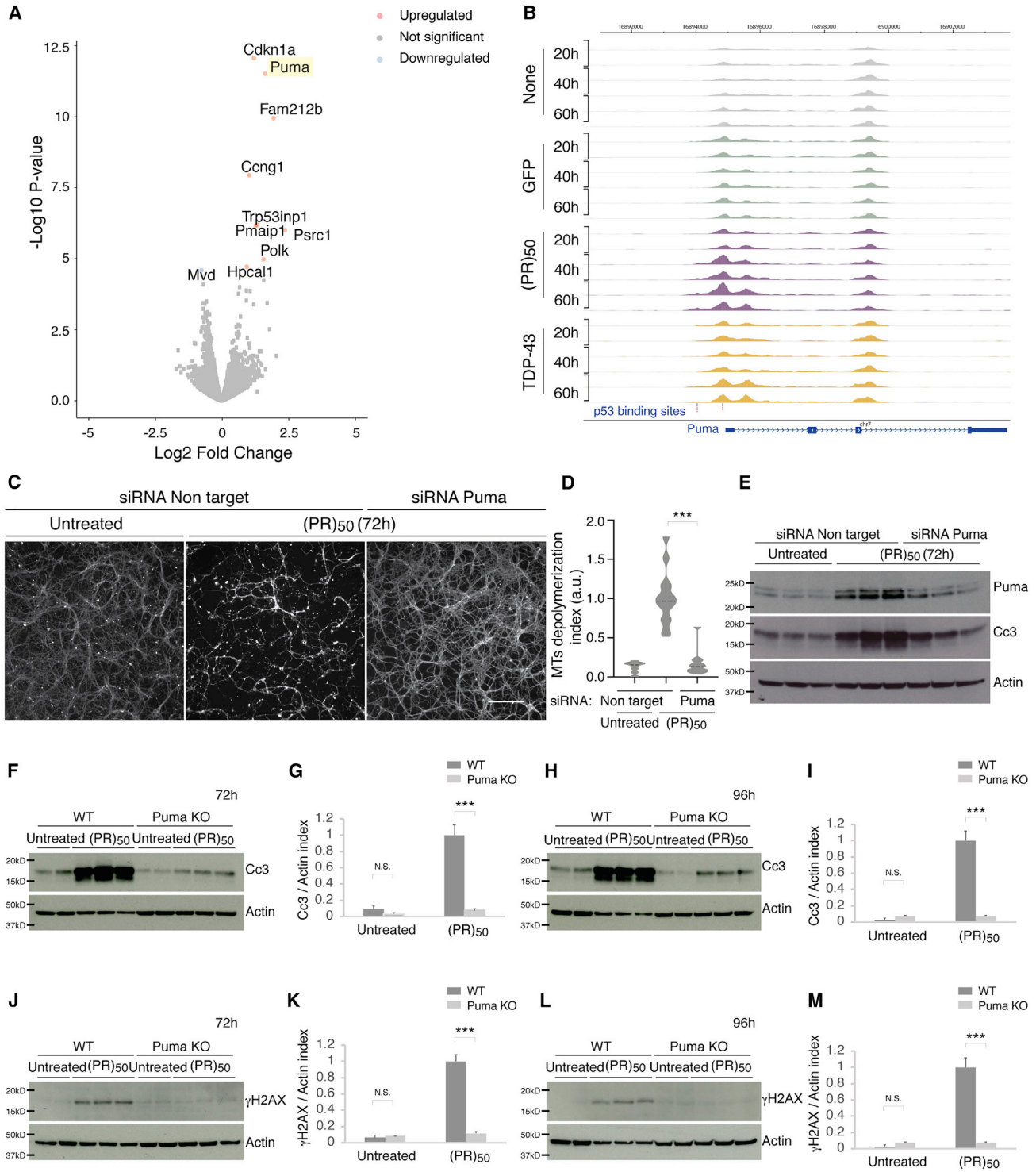

Figure 7. *Puma* ablation protects neurons from *C9orf72* $(PR)_{50}$-induced cell death and axonal degeneration

(A) Volcano plot of RNA-seq results from *C9orf72* $(PR)_{50}$- versus GFP-treated neurons at 40 h after treatment.

(B) Normalized ATAC-seq tracks at the *Puma* locus of neurons untreated or treated with GFP, $(PR)_{50}$, or TDP-43 at 20, 40, and 60 h.

(C–E) Cortical neurons were treated with siRNA against *Puma* or nontargeting control siRNA. Neurons were then treated with $(PR)_{50}$ for or left untreated. $(PR)_{50}$ induced degeneration in the nontargeting control treated neurons (C) and activated cleaved Caspase-3 (E). *Puma* reduction by siRNA (D) delayed $(PR)_{50}$ axonal

(legend continued on next page)

2017; Lopez-Gonzalez et al., 2016, 2019). Additional studies suggest that in ALS, motor neurons undergo an apoptotic mode of cell death (Akizuki et al., 2013; Eve et al., 2007; Martin, 2007; Ranganathan and Bowser, 2010; Sathasivam et al., 2001). Yet, this notion has also been challenged based on negative results, and recently, a form of programmed cell death termed "necroptosis" (programmed necrosis) was suggested to drive degeneration in ALS (He and Strong, 2000; Ito et al., 2016; Re et al., 2014; Yamazaki et al., 2005). Interestingly, ablating p53 in the SOD1 G93A transgenic mouse model had no statistically significant effect on disease onset, survival, or the extent of motor neuron degeneration (Kuntz et al., 2000). In addition, a recent study suggested that p53 plays a role in protein quality control, regulating clearance of mutant SOD1 and *C9orf72* DPRs (Lu et al., 2019). Given the extensive past research, it is surprising that there is no clear and simple answer to the question of what p53 does and whether it is a primary cause driving degeneration in ALS or rather a consequence of the degenerative process. We now provide evidence that p53 not only is robustly stabilized and activates a transcriptional program in response to *C9orf72* poly(PR) but also is required for neurodegeneration *in vitro* and *in vivo*. The ability of p53 reduction to rescue *C9orf72* mouse and fly models as well as iPSC motor neurons derived from *C9orf72* ALS patients suggests that p53 is one of the drivers of neurodegeneration caused by *C9orf72* mutations.

It is unlikely that activating p53 per se is sufficient to cause neurodegeneration. Because p53 is functionally inactivated in many human cancers, there has been interest in strategies to boost p53 levels or restore p53 activity to tumors as a cancer therapy. One way to do this is to inhibit MDM2, a negative regulator of p53 (Kubbutat et al., 1997). However, it might be dangerous to boost p53 levels in non-tumor cells, especially in tissues that are particularly sensitive to radiation and p53-induced apoptosis, like the intestinal crypts and thymus (Lowe et al., 1993; Potten et al., 1997). Indeed, using a genetic approach in mouse to restore p53 in the absence of MDM2 caused rapid cell death in thymus and gut epithelia (Ringshausen et al., 2006). Other approaches to increase p53 levels or activity resulted in diverse phenotypes ranging from developmental defects to embryonic lethality (Moyer et al., 2017; Van Nostrand and Attardi, 2014). Small-molecule approaches to target the MDM2/p53 interaction is another way to boost p53 levels. Two such inhibitors, Nutlin-3 (Vassilev et al., 2004) and MI-219 (Shangary and Wang, 2009) show selective toxicity to tumors. Importantly, results from both the genetic and chemical approaches suggest that systemic activation of p53 does not cause neurodegeneration in these animal models. Likewise, the consequence of systemic p53 activation has been analyzed in humans, both directly (e.g., whole-body irradiation or DNA-damage-inducing chemotherapeutics) and indirectly (by participating in clinical trials of MDM2/p53 small-molecule inhibitors), and so far, there is no direct evidence for it causing or increasing risk of ALS or FTD. Therefore, additional factors activated by *C9orf72* mutations may collaborate with p53 to drive neurodegeneration. Yet, other TFs might work together with p53 or even independently to mediate C9orf72 poly(PR) toxicity. Future efforts will focus on resolving the role of additional factors in collaborating with p53 to mediate C9orf72 poly(PR) toxicity and how this collaboration converges on the genome to activate transcription that result in neuronal cell death.

The surprising ability of p53 ablation to protect neurons from the toxic effects of *C9orf72* mutations, conferring complete protection *in vitro* from poly(PR) and partial protection from poly(GR) even after long-term culture and a >2.5-fold extension in lifespan *in vivo* from poly(PR), is intriguing. But is it reasonable to even consider p53 as a therapeutic target for ALS, given its important role as a tumor suppressor? There could be other ways to target p53's function in neurodegeneration without completely disabling its important activities, such as uncoupling p53's function in DNA damage repair from its function in tumor suppression (Brady et al., 2011). A vast number of post-translational modifications and interaction partners modulate p53 levels and activity. p53 is extensively modified by phosphorylation, acetylation, methylation, ubiquitylation, sumoylation, and neddylation (Boehme and Blattner, 2009; Meek and Anderson, 2009). The identification of the precise p53 modification profile in ALS will provide insights into the mechanism of p53 activity and its possible regulators and may suggest ways to target those modifications as a more specific therapeutic approach. Another approach could be to target the downstream effectors of p53-mediated neurodegeneration. We have identified at least one of these, Puma, which we show here to mediate p53-induced neurodegeneration caused by *C9orf72* $(PR)_{50}$. In contrast to p53, *Puma* KO mice are not inherently predisposed to develop spontaneous tumors (Jeffers et al., 2003; Valente et al., 2013; Villunger et al., 2003), raising the possibility of Puma-focused therapeutics.

Our application of genome-wide chromatin accessibility profiling on primary neurons has revealed a distinct and progressive signature of TF occupancy caused by *C9orf72* $(PR)_{50}$ that differs from TDP-43. This platform can be not only applied toward better understanding of molecular changes in ALS but also extended to other neurodegenerative diseases. A common feature to this heterogenous group of disorders is the accumulation of protein aggregates and the death of neurons affecting different parts of the CNS. This approach should provide insight

degeneration (C) and delayed cleaved caspase-3 activation (D). The extent of microtubule depolymerization (mean index) was calculated for each condition (D), as described in STAR methods (t test; ***$p < 0.001$). Scale bar, 100 μm.

(F–I) Cortical neurons from *Puma* KO embryos or their WT littermates were left untreated or treated with *C9orf72* $(PR)_{50}$ for 72 h (F and G) or 96 h (H and I). WT neurons treated with $(PR)_{50}$ resulted in increased cleaved caspase-3, which was reduced in the *Puma* KO neurons. Quantification of cleaved caspase-3 following $(PR)_{50}$ treatment was determined by immunoblotting and normalized to actin (G and I). Graphs show mean ± SEM (t test; ***$p < 0.001$; N.S., not significant).

(J–M) Cortical neurons from *Puma* KO embryos or their WT littermates were cultured for 3 days and either left untreated or treated with *C9orf72* $(PR)_{50}$ for an additional 72 h (J and K) or 96 h (L and M).

γH2AX levels were elevated after $(PR)_{50}$ treatment, and *Puma* ablation inhibited this induction at 72 h (J and K) and 96 h (L and M). Quantification of γH2AX following $(PR)_{50}$ treatment was determined by immunoblotting and normalized to actin (K and M). Graphs show mean ± SEM (t test; ***$p < 0.001$; N.S., not significant).

into chromatin regulation, TF binding, and epigenetic alterations that may underpin these neurodegenerative diseases.

STAR★METHODS

Detailed methods are provided in the online version of this paper and include the following:

- KEY RESOURCES TABLE
- RESOURCE AVAILABILITY
  - Lead contact
  - Materials availability
  - Data and code availability
- EXPERIMENTAL MODEL AND SUBJECT DETAILS
  - Mouse breeding and husbandry
  - Fly stocks and culture
  - Cell culture
  - Primary mouse cortical neurons
  - Motor neuron differentiation from iPSCs
- METHOD DETAILS
  - Neonatal viral injections
  - Mouse CNS histology
  - Fly eye degeneration experiment
  - Fly survival experiment
  - Neuron survival assay and ASO treatment
  - Lentiviral production
  - Comet assay
  - siRNA treatment
  - Immunoblotting
  - Immunocytochemistry
  - ATAC-seq
  - ATAC-seq analysis
  - RNA-seq
  - RNA-seq analysis
  - CRISPR-Cas9 screens in G401 cells
- QUANTIFICATION AND STATISTICAL ANALYSIS
  - Axonal quantification *in vitro*
  - Number of GFP, p53 positive cells and their colocalization
  - Axonal degeneration index
  - Statistical methods

ACKNOWLEDGMENTS

We thank Dr. Andrew Olson (Stanford Neuroscience Microscopy Service, supported by National Institutes of Health [NIH] grant NS069375). M.M.-N. is supported by an EMBO long-term fellowship (ALTF 301-2017), the SSSI-Muscular Dystrophy Association (M.M.-N.), and Stanford School of Medicine Dean's postdoctoral fellowships (M.M.-N.). This work was supported by NIH grants R35NS097263(10) (A.D.G.), R01NS094239 (T.E.L.), R01NS101986 (F.-B.G.), R37NS057553 (F.-B.G.), R35NS097273(17) (L.P.), P01NS084974 (L.P.), P01NS099114 (L.P.), R01NS089786 (M.T.L.), 1F32MH114620 (G.R.), K01AG049152 (J.S.Y.), R35CA197591 (L.D.A.), R01MH109912 (D.H.G.), R01NS097850 (J.K.I.), R01NS097850-01S1 (R.L.-G.), P50HG007735 (W.J.G.), R01HG008140 (W.J.G.), U19AI057266 (W.J.G.), UM1HG009442 (W.J.G.), and 1UM1HG009436 (W.J.G.); the Robert Packard Center for ALS Research at Johns Hopkins (A.D.G.); Target ALS (A.D.G., F.-B.G., J.C., L.P., and T.E.L.); the Blavatnik Family Foundation (J.A.B.); the Alzheimer's Association (2018-AARFD-592264 to G.R.L.); the Brain Rejuvenation Project of the Wu Tsai Neurosciences Institute (A.D.G.); the U.S. Department of Defense (grant W81XWH-15-1- 0187 to J.K.I.); the Merkin Family Foundation (J.K.I.); the New York Stem Cell Foundation (J.K.I.); the John Douglas French Alzheimer's Foundation; and the Tau Consortium (J.K.I.). J.K.I. is a New York Stem Cell Foundation Robertson Investigator and a Richard N. Merkin Scholar. W.J.G. is a Chan Zuckerberg Biohub investigator. Some of the computing for this project was performed on the Sherlock cluster. We would like to thank Stanford University and the Stanford Research Computing Center for providing computational resources and support that contributed to these research results. This work used the Genome Sequencing Service Center by Stanford Center for Genomics and Personalized Medicine Sequencing Center, supported by NIH grant S10OD020141. Some of the figures were created with BioRender.com.

AUTHOR CONTRIBUTIONS

Conceptualization, M.M.-N. and A.D.G.; Methodology, M.M.-N., Z.S., and A.N.; Investigation, M.M.-N., R.L.-G., L.N., Y.-J.Z., J.C., J.A.B., P.A.C., G.R.L., K.R., G.R., D.J.S., A.N., M.S., K.H., and N.S.-A.; Writing – Original Draft, M.M.-N. and A.D.G.; Writing – Review & Editing, M.M.-N., M.C.B., D.H.G., M.T.-L., L.D.A., T.E.L., J.K.I., F.-B.G., W.J.G., J.S.Y., L.P., and A.D.G.; Funding Acquisition, A.D.G.; Supervision, M.C.B., D.H.G., M.T.-L., L.D.A., T.E.L., J.K.I., F.-B.G., W.J.G., J.S.Y., L.P., and A.D.G.

DECLARATION OF INTERESTS

A.D.G. has served as a consultant for Aquinnah Pharmaceuticals, Prevail Therapeutics, and Third Rock Ventures and is a scientific founder of Maze Therapeutics. W.J.G. has affiliations with 10x Genomics (consultant), Guardant Health (consultant), and Protillion Biosciences (co-founder and consultant). J.K.I. is a co-founder of Acurastem. D.H.G has served as a consultant for Acurastem, Axial Biosciences, and Roche

Received: January 27, 2020
Revised: October 7, 2020
Accepted: December 15, 2020
Published: January 21, 2021

REFERENCES

Akizuki, M., Yamashita, H., Uemura, K., Maruyama, H., Kawakami, H., Ito, H., and Takahashi, R. (2013). Optineurin suppression causes neuronal cell death via NF-κB pathway. J. Neurochem. *126*, 699–704.

Ash, P.E., Bieniek, K.F., Gendron, T.F., Caulfield, T., Lin, W.L., Dejesus-Hernandez, M., van Blitterswijk, M.M., Jansen-West, K., Paul, J.W., 3rd, Rademakers, R., et al. (2013). Unconventional translation of C9ORF72 GGGGCC expansion generates insoluble polypeptides specific to c9FTD/ALS. Neuron *77*, 639–646.

Bae, B.I., Xu, H., Igarashi, S., Fujimuro, M., Agrawal, N., Taya, Y., Hayward, S.D., Moran, T.H., Montell, C., Ross, C.A., et al. (2005). p53 mediates cellular dysfunction and behavioral abnormalities in Huntington's disease. Neuron *47*, 29–41.

Barbosa, L.F., Cerqueira, F.M., Macedo, A.F., Garcia, C.C., Angeli, J.P., Schumacher, R.I., Sogayar, M.C., Augusto, O., Carrì, M.T., Di Mascio, P., and Medeiros, M.H. (2010). Increased SOD1 association with chromatin, DNA damage, p53 activation, and apoptosis in a cellular model of SOD1-linked ALS. Biochim. Biophys. Acta *1802*, 462–471.

Barry, S., Baird, G., Lascelles, K., Bunton, P., and Hedderly, T. (2011). Neurodevelopmental movement disorders - an update on childhood motor stereotypies. Dev. Med. Child Neurol. *53*, 979–985.

Belzil, V.V., Katzman, R.B., and Petrucelli, L. (2016). ALS and FTD: an epigenetic perspective. Acta Neuropathol. *132*, 487–502.

Berson, A., Sartoris, A., Nativio, R., Van Deerlin, V., Toledo, J.B., Porta, S., Liu, S., Chung, C.Y., Garcia, B.A., Lee, V.M., et al. (2017). TDP-43 promotes neurodegeneration by impairing chromatin remodeling. Curr. Biol. *27*, 3579–3590.e6.

Boehme, K.A., and Blattner, C. (2009). Regulation of p53—insights into a complex process. Crit. Rev. Biochem. Mol. Biol. *44*, 367–392.

Brady, C.A., and Attardi, L.D. (2010). p53 at a glance. J. Cell Sci. *123*, 2527–2532.

Brady, C.A., Jiang, D., Mello, S.S., Johnson, T.M., Jarvis, L.A., Kozak, M.M., Kenzelmann Broz, D., Basak, S., Park, E.J., McLaughlin, M.E., et al. (2011). Distinct p53 transcriptional programs dictate acute DNA-damage responses and tumor suppression. Cell *145*, 571–583.

Buenrostro, J.D., Giresi, P.G., Zaba, L.C., Chang, H.Y., and Greenleaf, W.J. (2013). Transposition of native chromatin for fast and sensitive epigenomic profiling of open chromatin, DNA-binding proteins and nucleosome position. Nat. Methods *10*, 1213–1218.

Buenrostro, J.D., Wu, B., Chang, H.Y., and Greenleaf, W.J. (2015). ATAC-seq: a method for assaying chromatin accessibility genome-wide. Curr. Protoc. Mol. Biol. *109*, 21.29.21–21.29.29.

Chesi, A., Staahl, B.T., Jovičić, A., Couthouis, J., Fasolino, M., Raphael, A.R., Yamazaki, T., Elias, L., Polak, M., Kelly, C., et al. (2013). Exome sequencing to identify de novo mutations in sporadic ALS trios. Nat. Neurosci. *16*, 851–855.

Chew, J., Gendron, T.F., Prudencio, M., Sasaguri, H., Zhang, Y.J., Castanedes-Casey, M., Lee, C.W., Jansen-West, K., Kurti, A., Murray, M.E., et al. (2015). Neurodegeneration. C9ORF72 repeat expansions in mice cause TDP-43 pathology, neuronal loss, and behavioral deficits. Science *348*, 1151–1154.

Cobos, S.N., Bennett, S.A., and Torrente, M.P. (2019). The impact of histone post-translational modifications in neurodegenerative diseases. Biochim. Biophys. Acta Mol. Basis Dis. *1865*, 1982–1991.

Cooper-Knock, J., Walsh, M.J., Higginbottom, A., Robin Highley, J., Dickman, M.J., Edbauer, D., Ince, P.G., Wharton, S.B., Wilson, S.A., Kirby, J., et al. (2014). Sequestration of multiple RNA recognition motif-containing proteins by C9orf72 repeat expansions. Brain *137*, 2040–2051.

Corces, M.R., Trevino, A.E., Hamilton, E.G., Greenside, P.G., Sinnott-Armstrong, N.A., Vesuna, S., Satpathy, A.T., Rubin, A.J., Montine, K.S., Wu, B., et al. (2017). An improved ATAC-seq protocol reduces background and enables interrogation of frozen tissues. Nat. Methods *14*, 959–962.

Cornwell, M., Vangala, M., Taing, L., Herbert, Z., Köster, J., Li, B., Sun, H., Li, T., Zhang, J., Qiu, X., et al. (2018). VIPER: Visualization Pipeline for RNA-seq, a Snakemake workflow for efficient and complete RNA-seq analysis. BMC Bioinformatics *19*, 135.

Coyne, A.N., Zaepfel, B.L., Hayes, L., Fitchman, B., Salzberg, Y., Luo, E.C., Bowen, K., Trost, H., Aigner, S., Rigo, F., et al. (2020). G_4C_2 repeat RNA initiates a POM121-mediated reduction in specific nucleoporins in C9orf72 ALS/FTD. Neuron *107*, 1124–1140.e11.

Culmsee, C., and Mattson, M.P. (2005). p53 in neuronal apoptosis. Biochem. Biophys. Res. Commun. *331*, 761–777.

Davidson, Y.S., Barker, H., Robinson, A.C., Thompson, J.C., Harris, J., Troakes, C., Smith, B., Al-Saraj, S., Shaw, C., Rollinson, S., et al. (2014). Brain distribution of dipeptide repeat proteins in frontotemporal lobar degeneration and motor neurone disease associated with expansions in C9ORF72. Acta Neuropathol. Commun. *2*, 70.

de la Monte, S.M., Sohn, Y.K., and Wands, J.R. (1997). Correlates of p53- and Fas (CD95)-mediated apoptosis in Alzheimer's disease. J. Neurol. Sci. *152*, 73–83.

de la Monte, S.M., Sohn, Y.K., Ganju, N., and Wands, J.R. (1998). P53- and CD95-associated apoptosis in neurodegenerative diseases. Lab. Invest. *78*, 401–411.

Deisenroth, C., Franklin, D.A., and Zhang, Y. (2016). The evolution of the ribosomal protein-MDM2-p53 pathway. Cold Spring Harb. Perspect. Med. *6*, 6.

DeJesus-Hernandez, M., Mackenzie, I.R., Boeve, B.F., Boxer, A.L., Baker, M., Rutherford, N.J., Nicholson, A.M., Finch, N.A., Flynn, H., Adamson, J., et al. (2011). Expanded GGGGCC hexanucleotide repeat in noncoding region of C9ORF72 causes chromosome 9p-linked FTD and ALS. Neuron *72*, 245–256.

Dobin, A., Davis, C.A., Schlesinger, F., Drenkow, J., Zaleski, C., Jha, S., Batut, P., Chaisson, M., and Gingeras, T.R. (2013). STAR: ultrafast universal RNA-seq aligner. Bioinformatics *29*, 15–21.

Donnelly, C.J., Zhang, P.W., Pham, J.T., Haeusler, A.R., Mistry, N.A., Vidensky, S., Daley, E.L., Poth, E.M., Hoover, B., Fines, D.M., et al. (2013). RNA toxicity from the ALS/FTD C9ORF72 expansion is mitigated by antisense intervention. Neuron *80*, 415–428.

Dull, T., Zufferey, R., Kelly, M., Mandel, R.J., Nguyen, M., Trono, D., and Naldini, L. (1998). A third-generation lentivirus vector with a conditional packaging system. J. Virol. *72*, 8463–8471.

el-Deiry, W.S., Tokino, T., Velculescu, V.E., Levy, D.B., Parsons, R., Trent, J.M., Lin, D., Mercer, W.E., Kinzler, K.W., and Vogelstein, B. (1993). WAF1, a potential mediator of p53 tumor suppression. Cell *75*, 817–825.

Eve, D.J., Dennis, J.S., and Citron, B.A. (2007). Transcription factor p53 in degenerating spinal cords. Brain Res. *1150*, 174–181.

Farg, M.A., Konopka, A., Soo, K.Y., Ito, D., and Atkin, J.D. (2017). The DNA damage response (DDR) is induced by the C9orf72 repeat expansion in amyotrophic lateral sclerosis. Hum. Mol. Genet. *26*, 2882–2896.

Fielder, E., von Zglinicki, T., and Jurk, D. (2017). The DNA damage response in neurons: die by apoptosis or survive in a senescence-like state? J. Alzheimers Dis. *60* (s1), S107–S131.

Gendron, T.F., Bieniek, K.F., Zhang, Y.J., Jansen-West, K., Ash, P.E., Caulfield, T., Daughrity, L., Dunmore, J.H., Castanedes-Casey, M., Chew, J., et al. (2013). Antisense transcripts of the expanded C9ORF72 hexanucleotide repeat form nuclear RNA foci and undergo repeat-associated non-ATG translation in c9FTD/ALS. Acta Neuropathol. *126*, 829–844.

Gendron, T.F., Belzil, V.V., Zhang, Y.J., and Petrucelli, L. (2014). Mechanisms of toxicity in C9FTLD/ALS. Acta Neuropathol. *127*, 359–376.

Gitler, A.D., and Tsuiji, H. (2016). There has been an awakening: emerging mechanisms of C9orf72 mutations in FTD/ALS. Brain Res. *1647*, 19–29.

Greenleaf, W.J. (2015). Assaying the epigenome in limited numbers of cells. Methods *72*, 51–56.

Han, J., Flemington, C., Houghton, A.B., Gu, Z., Zambetti, G.P., Lutz, R.J., Zhu, L., and Chittenden, T. (2001). Expression of bbc3, a pro-apoptotic BH3-only gene, is regulated by diverse cell death and survival signals. Proc. Natl. Acad. Sci. USA *98*, 11318–11323.

He, B.P., and Strong, M.J. (2000). Motor neuronal death in sporadic amyotrophic lateral sclerosis (ALS) is not apoptotic. A comparative study of ALS and chronic aluminium chloride neurotoxicity in New Zealand white rabbits. Neuropathol. Appl. Neurobiol. *26*, 150–160.

Hengartner, M.O. (2000). The biochemistry of apoptosis. Nature *407*, 770–776.

Idelman, G., Glaser, T., Roberts, C.T., Jr., and Werner, H. (2003). WT1-p53 interactions in insulin-like growth factor-I receptor gene regulation. J. Biol. Chem. *278*, 3474–3482.

Ito, Y., Ofengeim, D., Najafov, A., Das, S., Saberi, S., Li, Y., Hitomi, J., Zhu, H., Chen, H., Mayo, L., et al. (2016). RIPK1 mediates axonal degeneration by promoting inflammation and necroptosis in ALS. Science *353*, 603–608.

Jacks, T., Remington, L., Williams, B.O., Schmitt, E.M., Halachmi, S., Bronson, R.T., and Weinberg, R.A. (1994). Tumor spectrum analysis in p53-mutant mice. Curr. Biol. *4*, 1–7.

Jeffers, J.R., Parganas, E., Lee, Y., Yang, C., Wang, J., Brennan, J., MacLean, K.H., Han, J., Chittenden, T., Ihle, J.N., et al. (2003). Puma is an essential mediator of p53-dependent and -independent apoptotic pathways. Cancer Cell *4*, 321–328.

Kastenhuber, E.R., and Lowe, S.W. (2017). Putting p53 in context. Cell *170*, 1062–1078.

Kim, J.S., Lee, C., Bonifant, C.L., Ressom, H., and Waldman, T. (2007). Activation of p53-dependent growth suppression in human cells by mutations in PTEN or PIK3CA. Mol. Cell. Biol. *27*, 662–677.

Kim, G., Gautier, O., Tassoni-Tsuchida, E., Ma, X.R., and Gitler, A.D. (2020). ALS genetics: gains, losses, and implications for future therapies. Neuron *108*, 822–842.

Kitamura, Y., Shimohama, S., Kamoshima, W., Matsuoka, Y., Nomura, Y., and Taniguchi, T. (1997). Changes of p53 in the brains of patients with Alzheimer's disease. Biochem. Biophys. Res. Commun. *232*, 418–421.

Kitazumi, I., and Tsukahara, M. (2011). Regulation of DNA fragmentation: the role of caspases and phosphorylation. FEBS J. *278*, 427–441.

Kramer, N.J., Haney, M.S., Morgens, D.W., Jovičić, A., Couthouis, J., Li, A., Ousey, J., Ma, R., Bieri, G., Tsui, C.K., et al. (2018). CRISPR-Cas9 screens in human cells and primary neurons identify modifiers of C9ORF72 dipeptide-repeat-protein toxicity. Nat. Genet. *50*, 603–612.

Kubbutat, M.H., Jones, S.N., and Vousden, K.H. (1997). Regulation of p53 stability by Mdm2. Nature *387*, 299–303.

Kuntz, C., 4th, Kinoshita, Y., Beal, M.F., Donehower, L.A., and Morrison, R.S. (2000). Absence of p53: no effect in a transgenic mouse model of familial amyotrophic lateral sclerosis. Exp. Neurol. *165*, 184–190.

Kwon, I., Xiang, S., Kato, M., Wu, L., Theodoropoulos, P., Wang, T., Kim, J., Yun, J., Xie, Y., and McKnight, S.L. (2014). Poly-dipeptides encoded by the C9orf72 repeats bind nucleoli, impede RNA biogenesis, and kill cells. Science *345*, 1139–1145.

Langfelder, P., and Horvath, S. (2008). WGCNA: an R package for weighted correlation network analysis. BMC Bioinformatics *9*, 559.

Langmead, B., and Salzberg, S.L. (2012). Fast gapped-read alignment with Bowtie 2. Nat. Methods *9*, 357–359.

Law, J.C., Ritke, M.K., Yalowich, J.C., Leder, G.H., and Ferrell, R.E. (1993). Mutational inactivation of the p53 gene in the human erythroid leukemic K562 cell line. Leuk. Res. *17*, 1045–1050.

Lee, Y.B., Chen, H.J., Peres, J.N., Gomez-Deza, J., Attig, J., Stalekar, M., Troakes, C., Nishimura, A.L., Scotter, E.L., Vance, C., et al. (2013). Hexanucleotide repeats in ALS/FTD form length-dependent RNA foci, sequester RNA binding proteins, and are neurotoxic. Cell Rep. *5*, 1178–1186.

Levine, A.J., and Oren, M. (2009). The first 30 years of p53: growing ever more complex. Nat. Rev. Cancer *9*, 749–758.

Liao, Y., Smyth, G.K., and Shi, W. (2014). featureCounts: an efficient general purpose program for assigning sequence reads to genomic features. Bioinformatics *30*, 923–930.

Ling, S.C., Polymenidou, M., and Cleveland, D.W. (2013). Converging mechanisms in ALS and FTD: disrupted RNA and protein homeostasis. Neuron *79*, 416–438.

Lopez-Gonzalez, R., Lu, Y., Gendron, T.F., Karydas, A., Tran, H., Yang, D., Petrucelli, L., Miller, B.L., Almeida, S., and Gao, F.B. (2016). Poly(GR) in C9ORF72-related ALS/FTD compromises mitochondrial function and increases oxidative stress and DNA damage in iPSC-derived motor neurons. Neuron *92*, 383–391.

Lopez-Gonzalez, R., Yang, D., Pribadi, M., Kim, T.S., Krishnan, G., Choi, S.Y., Lee, S., Coppola, G., and Gao, F.B. (2019). Partial inhibition of the overactivated Ku80-dependent DNA repair pathway rescues neurodegeneration in *C9ORF72*-ALS/FTD. Proc. Natl. Acad. Sci. USA *116*, 9628–9633.

Love, M.I., Huber, W., and Anders, S. (2014). Moderated estimation of fold change and dispersion for RNA-seq data with DESeq2. Genome Biol. *15*, 550.

Lowe, S.W., Schmitt, E.M., Smith, S.W., Osborne, B.A., and Jacks, T. (1993). p53 is required for radiation-induced apoptosis in mouse thymocytes. Nature *362*, 847–849.

Lu, J., Periz, G., Lu, Y.N., Tang, Q., Liu, Y., Zhang, T., Shah, Y., Thombre, R., Aljumaah, R., Li, W., et al. (2019). L3MBTL1 regulates ALS/FTD-associated proteotoxicity and quality control. Nat. Neurosci. *22*, 875–886.

Mackenzie, I.R., Frick, P., Grässer, F.A., Gendron, T.F., Petrucelli, L., Cashman, N.R., Edbauer, D., Kremmer, E., Prudlo, J., Troost, D., and Neumann, M. (2015). Quantitative analysis and clinico-pathological correlations of different dipeptide repeat protein pathologies in C9ORF72 mutation carriers. Acta Neuropathol. *130*, 845–861.

Maor-Nof, M., Homma, N., Raanan, C., Nof, A., Hirokawa, N., and Yaron, A. (2013). Axonal pruning is actively regulated by the microtubule-destabilizing protein kinesin superfamily protein 2A. Cell Rep. *3*, 971–977.

Maor-Nof, M., Romi, E., Sar Shalom, H., Ulisse, V., Raanan, C., Nof, A., Leshkowitz, D., Lang, R., and Yaron, A. (2016). Axonal degeneration is regulated by a transcriptional program that coordinates expression of pro- and anti-degenerative factors. Neuron *92*, 991–1006.

Martin, L.J. (2000). p53 is abnormally elevated and active in the CNS of patients with amyotrophic lateral sclerosis. Neurobiol. Dis. *7* (6 Pt B), 613–622.

Martin, L.J. (2007). Transgenic mice with human mutant genes causing Parkinson's disease and amyotrophic lateral sclerosis provide common insight into mechanisms of motor neuron selective vulnerability to degeneration. Rev. Neurosci. *18*, 115–136.

Martin, L.J., and Wong, M. (2013). Aberrant regulation of DNA methylation in amyotrophic lateral sclerosis: a new target of disease mechanisms. Neurotherapeutics *10*, 722–733.

Meek, D.W., and Anderson, C.W. (2009). Posttranslational modification of p53: cooperative integrators of function. Cold Spring Harb. Perspect. Biol. *1*, a000950.

Mizielinska, S., Grönke, S., Niccoli, T., Ridler, C.E., Clayton, E.L., Devoy, A., Moens, T., Norona, F.E., Woollacott, I.O.C., Pietrzyk, J., et al. (2014). C9orf72 repeat expansions cause neurodegeneration in Drosophila through arginine-rich proteins. Science *345*, 1192–1194.

Morgens, D.W., Deans, R.M., Li, A., and Bassik, M.C. (2016). Systematic comparison of CRISPR/Cas9 and RNAi screens for essential genes. Nat. Biotechnol. *34*, 634–636.

Morgens, D.W., Wainberg, M., Boyle, E.A., Ursu, O., Araya, C.L., Tsui, C.K., Haney, M.S., Hess, G.T., Han, K., Jeng, E.E., et al. (2017). Genome-scale measurement of off-target activity using Cas9 toxicity in high-throughput screens. Nat. Commun. *8*, 15178.

Mori, K., Lammich, S., Mackenzie, I.R., Forné, I., Zilow, S., Kretzschmar, H., Edbauer, D., Janssens, J., Kleinberger, G., Cruts, M., et al. (2013a). hnRNP A3 binds to GGGGCC repeats and is a constituent of p62-positive/TDP43-negative inclusions in the hippocampus of patients with C9orf72 mutations. Acta Neuropathol. *125*, 413–423.

Mori, K., Weng, S.M., Arzberger, T., May, S., Rentzsch, K., Kremmer, E., Schmid, B., Kretzschmar, H.A., Cruts, M., Van Broeckhoven, C., et al. (2013b). The C9orf72 GGGGCC repeat is translated into aggregating dipeptide-repeat proteins in FTLD/ALS. Science *339*, 1335–1338.

Moyer, S.M., Larsson, C.A., and Lozano, G. (2017). Mdm proteins: critical regulators of embry ogenesis and homeostasis. J. Mol. Cell Biol. *9*, 16–25.

Nakano, K., and Vousden, K.H. (2001). PUMA, a novel proapoptotic gene, is induced by p53. Mol. Cell *7*, 683–694.

Neumann, M., Sampathu, D.M., Kwong, L.K., Truax, A.C., Micsenyi, M.C., Chou, T.T., Bruce, J., Schuck, T., Grossman, M., Clark, C.M., et al. (2006). Ubiquitinated TDP-43 in frontotemporal lobar degeneration and amyotrophic lateral sclerosis. Science *314*, 130–133.

Ni, J.Q., Zhou, R., Czech, B., Liu, L.P., Holderbaum, L., Yang-Zhou, D., Shim, H.S., Tao, R., Handler, D., Karpowicz, P., et al. (2011). A genome-scale shRNA resource for transgenic RNAi in Drosophila. Nat. Methods *8*, 405–407.

Nikolayeva, O., and Robinson, M.D. (2014). edgeR for differential RNA-seq and ChIP-seq analysis: an application to stem cell biology. Methods Mol. Biol. *1150*, 45–79.

Olive, P.L., and Banáth, J.P. (2006). The comet assay: a method to measure DNA damage in individual cells. Nat. Protoc. *1*, 23–29.

Otsu, N. (1979). A threshold selection method from Gray-level histograms. IEEE Trans. Syst. Man Cybern. *9*, 62–66.

Periz, G., Lu, J., Zhang, T., Kankel, M.W., Jablonski, A.M., Kalb, R., McCampbell, A., and Wang, J. (2015). Regulation of protein quality control by UBE4B and LSD1 through p53-mediated transcription. PLoS Biol. *13*, e1002114.

Potten, C.S., Wilson, J.W., and Booth, C. (1997). Regulation and significance of apoptosis in the stem cells of the gastrointestinal epithelium. Stem Cells *15*, 82–93.

Qiu, H., Lee, S., Shang, Y., Wang, W.Y., Au, K.F., Kamiya, S., Barmada, S.J., Finkbeiner, S., Lui, H., Carlton, C.E., et al. (2014). ALS-associated mutation

FUS-R521C causes DNA damage and RNA splicing defects. J. Clin. Invest. *124*, 981–999.

Ranganathan, S., and Bowser, R. (2010). p53 and cell cycle proteins participate in spinal motor neuron cell death in ALS. Open Pathol. J. *4*, 11–22.

Re, D.B., Le Verche, V., Yu, C., Amoroso, M.W., Politi, K.A., Phani, S., Ikiz, B., Hoffmann, L., Koolen, M., Nagata, T., et al. (2014). Necroptosis drives motor neuron death in models of both sporadic and familial ALS. Neuron *81*, 1001–1008.

Reimand, J., Kull, M., Peterson, H., Hansen, J., and Vilo, J. (2007). g:Profiler—a web-based toolset for functional profiling of gene lists from large-scale experiments. Nucleic Acids Res. *35*, W193-200.

Renton, A.E., Majounie, E., Waite, A., Simón-Sánchez, J., Rollinson, S., Gibbs, J.R., Schymick, J.C., Laaksovirta, H., van Swieten, J.C., Myllykangas, L., et al.; ITALSGEN Consortium (2011). A hexanucleotide repeat expansion in C9ORF72 is the cause of chromosome 9p21-linked ALS-FTD. Neuron *72*, 257–268.

Ringshausen, I., O'Shea, C.C., Finch, A.J., Swigart, L.B., and Evan, G.I. (2006). Mdm2 is critically and continuously required to suppress lethal p53 activity in vivo. Cancer Cell *10*, 501–514.

Ritson, G.P., Custer, S.K., Freibaum, B.D., Guinto, J.B., Geffel, D., Moore, J., Tang, W., Winton, M.J., Neumann, M., Trojanowski, J.Q., et al. (2010). TDP-43 mediates degeneration in a novel Drosophila model of disease caused by mutations in VCP/p97. J. Neurosci. *30*, 7729–7739.

Rogakou, E.P., Nieves-Neira, W., Boon, C., Pommier, Y., and Bonner, W.M. (2000). Initiation of DNA fragmentation during apoptosis induces phosphorylation of H2AX histone at serine 139. J. Biol. Chem. *275*, 9390–9395.

Saberi, S., Stauffer, J.E., Jiang, J., Garcia, S.D., Taylor, A.E., Schulte, D., Ohkubo, T., Schloffman, C.L., Maldonado, M., Baughn, M., et al. (2018). Sense-encoded poly-GR dipeptide repeat proteins correlate to neurodegeneration and uniquely co-localize with TDP-43 in dendrites of repeat-expanded C9orf72 amyotrophic lateral sclerosis. Acta Neuropathol. *135*, 459–474.

Sakae, N., Bieniek, K.F., Zhang, Y.J., Ross, K., Gendron, T.F., Murray, M.E., Rademakers, R., Petrucelli, L., and Dickson, D.W. (2018). Poly-GR dipeptide repeat polymers correlate with neurodegeneration and Clinicopathological subtypes in C9ORF72-related brain disease. Acta Neuropathol. Commun. *6*, 63.

Sareen, D., O'Rourke, J.G., Meera, P., Muhammad, A.K., Grant, S., Simpkinson, M., Bell, S., Carmona, S., Ornelas, L., Sahabian, A., et al. (2013). Targeting RNA foci in iPSC-derived motor neurons from ALS patients with a C9ORF72 repeat expansion. Sci. Transl. Med. *5*, 208ra149.

Sathasivam, S., Ince, P.G., and Shaw, P.J. (2001). Apoptosis in amyotrophic lateral sclerosis: a review of the evidence. Neuropathol. Appl. Neurobiol. *27*, 257–274.

Schep, A.N., Wu, B., Buenrostro, J.D., and Greenleaf, W.J. (2017). chromVAR: inferring transcription-factor-associated accessibility from single-cell epigenomic data. Nat. Methods *14*, 975–978.

Schludi, M.H., May, S., Grässer, F.A., Rentzsch, K., Kremmer, E., Küpper, C., Klopstock, T., Arzberger, T., and Edbauer, D.; German Consortium for Frontotemporal Lobar Degeneration; Bavarian Brain Banking Alliance (2015). Distribution of dipeptide repeat proteins in cellular models and C9orf72 mutation cases suggests link to transcriptional silencing. Acta Neuropathol. *130*, 537–555.

Shangary, S., and Wang, S. (2009). Small-molecule inhibitors of the MDM2-p53 protein-protein interaction to reactivate p53 function: a novel approach for cancer therapy. Annu. Rev. Pharmacol. Toxicol. *49*, 223–241.

Shi, Y., Lin, S., Staats, K.A., Li, Y., Chang, W.H., Hung, S.T., Hendricks, E., Linares, G.R., Wang, Y., Son, E.Y., et al. (2018). Haploinsufficiency leads to neurodegeneration in C9ORF72 ALS/FTD human induced motor neurons. Nat. Med. *24*, 313–325.

Simon, D.J., Pitts, J., Hertz, N.T., Yang, J., Yamagishi, Y., Olsen, O., Tešić Mark, M., Molina, H., and Tessier-Lavigne, M. (2016). Axon degeneration gated by retrograde activation of somatic pro-apoptotic signaling. Cell *164*, 1031–1045.

Soussi, T. (2000). The p53 tumor suppressor gene: from molecular biology to clinical investigation. Ann. N Y Acad. Sci. *910*, 121–137, discussion 137–139.

Sturm, M., Schroeder, C., and Bauer, P. (2016). SeqPurge: highly-sensitive adapter trimming for paired-end NGS data. BMC Bioinformatics *17*, 208.

Szybińska, A., and Leśniak, W. (2017). P53 dysfunction in neurodegenerative diseases: the cause or effect of pathological changes? Aging Dis. *8*, 506–518.

Tao, Z., Wang, H., Xia, Q., Li, K., Li, K., Jiang, X., Xu, G., Wang, G., and Ying, Z. (2015). Nucleolar stress and impaired stress granule formation contribute to C9orf72 RAN translation-induced cytotoxicity. Hum. Mol. Genet. *24*, 2426–2441.

Valente, L.J., Gray, D.H., Michalak, E.M., Pinon-Hofbauer, J., Egle, A., Scott, C.L., Janic, A., and Strasser, A. (2013). p53 efficiently suppresses tumor development in the complete absence of its cell-cycle inhibitory and proapoptotic effectors p21, Puma, and Noxa. Cell Rep. *3*, 1339–1345.

Van Nostrand, J.L., and Attardi, L.D. (2014). Guilty as CHARGED: p53's expanding role in disease. Cell Cycle *13*, 3798–3807.

Vassilev, L.T., Vu, B.T., Graves, B., Carvajal, D., Podlaski, F., Filipovic, Z., Kong, N., Kammlott, U., Lukacs, C., Klein, C., et al. (2004). In vivo activation of the p53 pathway by small-molecule antagonists of MDM2. Science *303*, 844–848.

Villunger, A., Michalak, E.M., Coultas, L., Müllauer, F., Böck, G., Ausserlechner, M.J., Adams, J.M., and Strasser, A. (2003). p53- and drug-induced apoptotic responses mediated by BH3-only proteins puma and noxa. Science *302*, 1036–1038.

Vogt, M.A., Ehsaei, Z., Knuckles, P., Higginbottom, A., Helmbrecht, M.S., Kunath, T., Eggan, K., Williams, L.A., Shaw, P.J., Wurst, W., et al. (2018). TDP-43 induces p53-mediated cell death of cortical progenitors and immature neurons. Sci. Rep. *8*, 8097.

Wang, W.Y., Pan, L., Su, S.C., Quinn, E.J., Sasaki, M., Jimenez, J.C., Mackenzie, I.R., Huang, E.J., and Tsai, L.H. (2013). Interaction of FUS and HDAC1 regulates DNA damage response and repair in neurons. Nat. Neurosci. *16*, 1383–1391.

Wen, X., Tan, W., Westergard, T., Krishnamurthy, K., Markandaiah, S.S., Shi, Y., Lin, S., Shneider, N.A., Monaghan, J., Pandey, U.B., et al. (2014). Antisense proline-arginine RAN dipeptides linked to C9ORF72-ALS/FTD form toxic nuclear aggregates that initiate in vitro and in vivo neuronal death. Neuron *84*, 1213–1225.

White, M.R., Mitrea, D.M., Zhang, P., Stanley, C.B., Cassidy, D.E., Nourse, A., Phillips, A.H., Tolbert, M., Taylor, J.P., and Kriwacki, R.W. (2019). C9orf72 poly(PR) dipeptide repeats disturb biomolecular phase separation and disrupt nucleolar function. Mol. Cell *74*, 713–728.e6.

Wils, H., Kleinberger, G., Janssens, J., Pereson, S., Joris, G., Cuijt, I., Smits, V., Ceuterick-de Groote, C., Van Broeckhoven, C., and Kumar-Singh, S. (2010). TDP-43 transgenic mice develop spastic paralysis and neuronal inclusions characteristic of ALS and frontotemporal lobar degeneration. Proc. Natl. Acad. Sci. USA *107*, 3858–3863.

Xu, Z., Poidevin, M., Li, X., Li, Y., Shu, L., Nelson, D.L., Li, H., Hales, C.M., Gearing, M., Wingo, T.S., and Jin, P. (2013). Expanded GGGGCC repeat RNA associated with amyotrophic lateral sclerosis and frontotemporal dementia causes neurodegeneration. Proc. Natl. Acad. Sci. USA *110*, 7778–7783.

Yamada, S.B., Gendron, T.F., Niccoli, T., Genuth, N.R., Grosely, R., Shi, Y., Glaria, I., Kramer, N.J., Nakayama, L., Fang, S., et al. (2019). RPS25 is required for efficient RAN translation of C9orf72 and other neurodegenerative disease-associated nucleotide repeats. Nat. Neurosci. *22*, 1383–1388.

Yamazaki, M., Esumi, E., and Nakano, I. (2005). Is motoneuronal cell death in amyotrophic lateral sclerosis apoptosis? Neuropathology *25*, 381–387.

Yang, K., Yang, J., and Yi, J. (2018). Nucleolar stress: hallmarks, sensing mechanism and diseases. Cell Stress *2*, 125–140.

Yu, J., Zhang, L., Hwang, P.M., Kinzler, K.W., and Vogelstein, B. (2001). PUMA induces the rapid apoptosis of colorectal cancer cells. Mol. Cell *7*, 673–682.

Zhang, Y., Liu, T., Meyer, C.A., Eeckhoute, J., Johnson, D.S., Bernstein, B.E., Nusbaum, C., Myers, R.M., Brown, M., Li, W., and Liu, X.S. (2008). Model-based analysis of ChIP-seq (MACS). Genome Biol. *9*, R137.

Zhang, K., Donnelly, C.J., Haeusler, A.R., Grima, J.C., Machamer, J.B., Steinwald, P., Daley, E.L., Miller, S.J., Cunningham, K.M., Vidensky, S., et al. (2015). The C9orf72 repeat expansion disrupts nucleocytoplasmic transport. Nature *525*, 56–61.

Zhang, Y.J., Guo, L., Gonzales, P.K., Gendron, T.F., Wu, Y., Jansen-West, K., O'Raw, A.D., Pickles, S.R., Prudencio, M., Carlomagno, Y., et al. (2019). Heterochromatin anomalies and double-stranded RNA accumulation underlie *C9orf72* poly(PR) toxicity. Science *363*, 363.

Zhaunova, L., Ohkura, H., and Breuer, M. (2016). Kdm5/Lid regulates chromosome architecture in meiotic prophase I independently of its histone demethylase activity. PLoS Genet. *12*, e1006241.

Zu, T., Liu, Y., Bañez-Coronel, M., Reid, T., Pletnikova, O., Lewis, J., Miller, T.M., Harms, M.B., Falchook, A.E., Subramony, S.H., et al. (2013). RAN proteins and RNA foci from antisense transcripts in C9ORF72 ALS and frontotemporal dementia. Proc. Natl. Acad. Sci. USA *110*, E4968–E4977.

STAR★METHODS

KEY RESOURCES TABLE

REAGENT or RESOURCE	SOURCE	IDENTIFIER
Antibodies		
Tubulin β-III	Covance	Cat# 801201; RRID:AB_2313773
p53	Leica Biosystems	Cat# p53-CM5P-L; RRID:AB_2744683
p53	Cell Signaling	Cat# 2524; RRID: AB_331743
p53	Cell Signaling	Cat# 2527; RRID:AB_10695803
Phospho-p53 (ser15)	Cell Signaling	Cat# 9284; RRID:AB_331464
NeuN	Millipore Sigma	Cat# MAB377; RRID: AB_2298772
Cleaved Caspase-3	Cell Signaling	Cat# 9662; RRID:AB_331439
Flag	Millipore Sigma	Cat# F1804; RRID:AB_262044
phospho-Histone H2A.X (Ser139)	Millipore Sigma	Cat# 05-636; RRID:AB_309864
Actin	Millipore Sigma	Cat# MAB1501; RRID:AB_2223041
GAPDH	Millipore Sigma	Cat# G8795; RRID:AB_1078991
C9ORF72/C9RANT (Poly-GR)	Millipore Sigma	Cat# ABN1361;
TDP-43 C-terminal	Millipore Sigma	Cat# T1580; RRID:AB_2532125
Bacterial and virus strains		
AAV9-CMV-enhanced chicken β-actin-GFP-$(PR)_{50}$	Zhang et al., 2019	N/A
AAV9-CMV-enhanced chicken β-actin-GFP	Zhang et al., 2019	N/A
Lenti-syn-$(PR)_{50}$	Kramer et al., 2018	N/A
Lenti-syn-(GFP)	Kramer et al., 2018	N/A
Lenti-syn-$(GR)_{50}$	This paper	N/A
Lenti-syn-TDP-43	This paper	N/A
pLKO-p53-shRNA-427	Kim et al., 2007	Addgene 25636;
pMDLg/pRRE	Dull et al., 1998	Addgene 12251;
pRSV-ReV	Dull et al., 1998	Addgene 12253;
pMD2.0	Dull et al., 1998	Addgene 12259;
Chemicals, peptides, and recombinant proteins		
Cycloheximide	Sigma-Aldrich	01810-1G; CAS 66-81-9
Critical commercial assays		
RNeasy Plus Micro Kit	QIAGEN	74034
SureSelect Strand-Specific RNA Library Preparation kit	Illumina	G9691-90010
NextSeq 500/550 v2 Kits HighOutput 150cycles	Illumina	FC-404-2002
Nextera DNA Library Preparation Kit	Illumina	FC-121-1030

(*Continued on next page*)

Continued

REAGENT or RESOURCE	SOURCE	IDENTIFIER
Deposited data		
Raw and analyzed data	This paper	GEO: GSE162048
Experimental models: cell lines		
293T	ATCC	CRL-3216
G401	ATCC	CRL-1441
iMN generated from human lymphocytes from healthy subjects	Coriell Institute	ND03231
iMN generated from human lymphocytes from healthy subjects	Coriell Institute	ND03719
iMN generated from human lymphocytes from healthy subjects	Coriell Institute	ND05280
iMN generated from human lymphocytes from ALS patients	Coriell Institute	ND06769
iMN generated from human lymphocytes from ALS patients	Coriell Institute	ND10689
iMN generated from human lymphocytes from ALS patients	Coriell Institute	ND12099
C9ORF72 iPSC line #1	Lopez-Gonzalez et al., 2019	26L6
C9ORF72 iPSC line #2	Lopez-Gonzalez et al., 2019	27L11
C9ORF72 iPSC line #1 'corrected'	Lopez-Gonzalez et al., 2019	26Z90
C9ORF72 iPSC line #2 'corrected'	Lopez-Gonzalez et al., 2019	27M91
Experimental models: organisms/strains		
Mouse: B6.129S2-Trp53tm1Tyj/J	The Jackson Laboratory	JAX: 002101
Mouse: C57BL/6-Bbc3tm1Ast/J	The Jackson Laboratory	JAX: 011067
Mouse: B6;SJL-Tg(Thy1-TARDBP)4Singh/J	The Jackson Laboratory	JAX: 012836
Mouse: C57BL/6J	The Jackson Laboratory	JAX:100012
D. melanogaster P{TRiP.GL01032}attP2	FlyBase	FBti0146570
D. melanogaster P{TRiP.GL01220}attP40	FlyBase	FBti0149303
D. melanogaster P{TRiP.HMS02286}attP2	FlyBase	FBti0149916
Oligonucleotides		
ON-TARGETplus Mouse Trp53 siRNA	Horizon Technology	L-040642-00-0005
ON-TARGETplus Mouse Trp63 siRNA	Horizon Technology	L-040654-00-0005
ON-TARGETplus Mouse Trp73 siRNA	Horizon Technology	L-043871-00-0005
ON-TARGETplus Mouse Bbc3 siRNA	Horizon Technology	L-050032-00-0005
ON-TARGETplus Non-target siRNA	Horizon Technology	D-001810-10-20
ASO1 targeting sequence: mA*mG*mC*mU*mG* T*T*C*C*G*T*C*C*C*A*mG*mU*mA*mG*mA	Integrated DNA Technologies	N/A
ASO2 targeting sequence: mG*mU*mC*mA*mU*C* C*A*A*A*T*A*C*T*C*mC*mA*mC*mA*mC	Integrated DNA Technologies	N/A
ASO control sequence: mG*mC*mG* mA*mC*T* A*T*A* C*G*C* G*C*A* mA*mU*mA* mU*mG	Integrated DNA Technologies	N/A
Software and algorithms		
Analysis code	This paper	https://github.com/zshipony/Maor_Nof_2020
Image processing (Axonal_Quantification)	This paper	https://github.com/nofaviv/Axonal_Quantification
Image processing (Axonal_degeneration)	This paper	https://github.com/nofaviv/Axonal_Degeneration
Image processing (Co-localization)	This paper	https://github.com/nofaviv/Cells_CoLocalization
RNaseq analysis	Kramer et al., 2018	https://github.com/emc2cube/Bioinformatics/blob/master/sh_RNAseq.sh
CRISPR screen analysis	Kramer et al., 2018	https://github.com/emc2cube/Bioinformatics/blob/master/sh_CRISPR.sh

RESOURCE AVAILABILITY

Lead contact

Further information and requests for resources and reagents should be directed to and will be fulfilled by the Lead Contact, Aaron D. Gitler (agitler@stanford.edu).

Materials availability

All unique/stable reagents generated in this study are available from the Lead Contact without restriction.

Data and code availability

Original data have been deposited to GEO:GSE162048.

All code generated during this study for the ATACseq and RNaseq analysis are available at (https://github.com/zshipony/Maor_Nof_2020). All algorithms and code generated for image processing are available at (https://github.com/nofaviv/Axonal_Quantification, https://github.com/nofaviv/Axonal_Degeneration, https://github.com/nofaviv/Cells_CoLocalization).

EXPERIMENTAL MODEL AND SUBJECT DETAILS

Mouse breeding and husbandry

Animals were bred and used as approved by the Administrative Panel of Laboratory Animal Care (APLAC) of Stanford University, an institution accredited by the Association for the Assessment and Accreditation of Laboratory Animal Care (AAALAC). Mouse breeding and husbandry Mice (male and female) were between the ages of P0 and P400; Animals (5 mice per cage) were provided food and water and were maintained on a regular 12-h light–dark cycle. Embryos were harvested from pregnant dams at stage E16.5. Wild-type cultures were generated from C57BL/6 mice. For mutant strains, comparisons between wild-type and mutant embryos derive from the same pregnant female. Knockout strains used in this study are summarized in the Key Resources Table. Mice were maintained on a C57BL/6J hybrid background by crossing with F1 mice from JAX to propagate the strain (stock no: 100012, C57BL/6J).

Fly stocks and culture

Flies were maintained on a cornmeal–molasses–yeast medium and at room temperature (22°C) with 60%–65% humidity. The following *Drosophila* lines were obtained from the Bloomington Stock Center: UAS-LacZ, UAS-mCherry-RNAi, UAS-emb-RNAi, GMR-GAL4, and OK371-GAL4. The UAS-p53.ORF.3xHA was obtained from FlyORF. The UAS-(G4C2)30 lines were obtained from Dr Peng Jin's laboratory (Xu et al., 2013). The three p53 RNAi lines used in this study are summarized in the key resources table.

Cell culture

G401 cells (ATCC) were cultured in RPMI-1640 (GIBCO) media with 10% fetal bovine serum (FBS) (Hyclone), penicillin (10,000 I.U./mL), streptomycin (10,000 μg/mL), and L-glutamine (2 mM). Cells were grown in log phase by maintaining the population at a concentration of 500,000 cells per mL. HEK293T (ATCC) cells were cultured in DMEM, 10% fetal bovine serum (FBS), penicillin (10,000 I.U./mL) and streptomycin (10,000 μg/mL). G401 and HEK293T cells were maintained in a controlled humidified incubator at 37°C, with 5% CO2.

Primary mouse cortical neurons

Primary mouse cortical neurons were dissociated into single-cell suspensions from E16.5 mouse cortices with a papain dissociation system (Worthington Biochemical Corporation). Neurons were seeded onto poly-L-lysine–coated plates (0.1% (wt/vol)) and grown in Neurobasal medium (GIBCO) supplemented with B-27 serum-free supplement (GIBCO), GlutaMAX, and penicillin–streptomycin (GIBCO) in a humidified incubator at 37 °C, with 5% CO2. Half media changes were performed every 4 or 5 days, or as required. Neurons were plated on 12mm glass coverslips (Carolina Biological Supplies cat# 633009) in 24-well plates (350,000 cells/well) and in 12-well plates for DNA, RNA and protein extraction (450,000 cells/well).

Motor neuron differentiation from iPSCs

Differentiation of iPSCs into motor neurons was performed as described in (Lopez-Gonzalez et al., 2019). The C9ORF72 iPSC lines and their isogenic controls used in this study are summarized in the Key Resources Table. The iPSCs were plated and expanded in mTSER1 medium (Stem Cell Technologies) in Matrigel-coated wells. One day after plating, the culture medium was replaced with neuroepithelial progenitor (NEP) medium, DMEM/F12, neurobasal medium at 1:1, 0.5X N2, 0.5X B27, 0.1 mM ascorbic acid (Sigma), 1X Glutamax (Invitrogen), 3 μM CHIR99021 (Tocris Bioscience), 2 μM DMH1 (Tocris Bioscience), and 2 μM SB431542 (Stemgent). After 6 days, NEPs were dissociated with accutase, split 1:6 into Matrigel-coated wells, and cultured for 6 days in motor neuron progenitor induction medium (NEP with 0.1 μM retinoic acid and 0.5 μM purmorphamine, both from Stemgent). Motor neuron progenitors were dissociated with accutase to generate neurosphere suspension cultures supplemented with NEP plus 0.5 μM retinoic acid and 0.1 μM purmorphamine. After 6 days, neurospheres were dissociated into single cells, plated on laminin-coated

plates/coverslips in motor neuron differentiation medium containing 0.5 μM retinoic acid, 0.1 μM purmorphamine, and 0.1 μM Compound E (Calbiochem) for 2 weeks and then in the same medium without Compound E for up to 2 and half months.

An additional panel of induced motor neurons (iMNs) was generated as previously described (Shi et al., 2018). Cells were purchased from Coriell Institute. The panel of control lines and the panel of C9ORF72 ALS lines are summarized in the Key Resources Table. Human secondary fibroblasts were transduced with a cocktail of transcription factors that consisted of Ascl1, Brn2, Isl1, Lhx3, Ngn2, NeuroD1, and Mytl1 using retrovirus. The following day Hb9::RFP+ lentivirus was added to the fibroblast cultures. On Day 4, primary glia isolated from male and female ICR mouse pups (P2-P3) were added to the cultures in glia medium. To induce the formation of neurons, the media was switched the following day to N3 media consisting of DMEM/F-12 (Life Technologies), 2% FBS, B-27 and N2 supplements (Life Technologies), 1% Penicillin/Streptomycin, 7.5 μM Rep Sox (Selleck), and 10 ng/ml each of GDNF, BDNF, CNTF, and FGF (R&D). The culture media was fully replenished every 2 days, until 14 days post-transduction.

METHOD DETAILS

Neonatal viral injections

GFP and GFP-$(PR)_{50}$ were generated as described previously (Zhang et al., 2019). Intracerebroventricular (ICV) injections of AAV were performed as previously described with some minor modifications (Chew et al., 2015; Zhang et al., 2019). Briefly, a 32-gauge needle (Hamilton Company) attached to a 10 μl syringe (Hamilton Company) was inserted at approximately two-fifths the distance between lambda suture and each eye of the pups at post-natal day 0, after they were cryo anesthetized on ice for approximately 3 minutes or until pups exhibited no movement. The needle was inserted at a 30-degree angle from the surface of the head and held at a depth of approximately two millimeters. 2 μl (1E10 genomes/μl) of AAV9-GFP or AAV9-GFP-$(PR)_{50}$ solution per cerebral ventricle was manually injected into each cerebral ventricle. After injections, pups were placed on a heat pad until they completely recovered from anesthesia and then were placed back into their home cages.

Mouse CNS histology

Anesthetized mice were perfused with PBS and the brain and spinal cord were carefully dissected and washed in chilled PBS. The brains as well as the cervical and lumbar enlargements of the spinal cord were placed in 4% PFA in PBS at 4°C for 48h and then stored in 30% sucrose in PBS. PFA-fixed brains were mounted in OCT and cut to a thickness of 40 μm (coronal sections) using a Leica CM3050 S Cryostat with a cryo-microtome (Leica) and stored in cryoprotective medium (30% glycerol, 30% ethylene glycol) at − 20°C. Washes were done 4 times for 5 min each in TBST (0.1% Tween-20), unless otherwise noted, at RT. Washes and incubation steps were performed with gentle rotation using an orbital rotator. The sections were stained using immunofluorescence. The sections were washed then blocked/pre-treated in TBST with 0.1% triton-X and 10% normal goat or donkey serum (depending on secondary antibody host) for 1h at RT. Primary antibodies were diluted in TBST with 10% serum at 4°C overnight. The sections were then washed, treated with Alexa Fluor conjugated secondary antibodies (Life Technologies) diluted at 1:1000 in TBST with 10% serum for 3h, and washed again with DAPI (1:5000) added to the final wash. Sections were mounted on frosted slides in PB using a paintbrush, and when the sections were no longer visibly wet, the slides were coverslipped using Prolong diamond antifade mountant (Molecular Probes). High quality images were taken on a Zeiss LSM 710 Confocal Scope.

Fly eye degeneration experiment

UAS-(G4C2)30 flies recombined with GMR-Gal4 were selected as male parental flies for crossing (♀w1118 x ♂GMR-Gal4; UAS-(G4C2)30/CyO). Overexpressing 30 Hexanucleotide Repeat Expansion (HRE) in all photoreceptors using GMR-Gal4 causes eye degeneration in adult flies during aging. Eyes degeneration score were examined based on Dr. Paul Taylor's study (Ritson et al., 2010). It was quantified for the presence of supernumerary inter-ommatidial bristles (IOBs), IOBs with abnormal orientation, necrotic patches, a decrease in size, retinal collapse, fusion of ommatidia, disorganization of ommatidial array and loss of pigmentation in adult male progeny. Points were added if: there was complete loss of IOBs (+1), more than 3 small or 1 large necrotic patch (+1), retinal collapse extended to the midline of the eye (+1) or beyond (+2), loss of ommatidial structure in less than 50% (+1) or more than 50% (+2) of the eye, and if pigmentation loss resulted in change of eye color from red to orange (+1) or pale orange/white (+2). Images were taken on a Zeiss LSM800 Airyscan laser scanning confocal microscope. Image quantification were carried with ImageJ.

Fly survival experiment

UAS-(G4C2)30 flies recombined with OK371-Gal4 were selected as male parental flies for crossing (♀w1118 x ♂OK371-Gal4; UAS-(G4C2)30/TM6B, GAL80). Overexpressing 30 HRE in fly motor neurons using OK371-Gal4 causes lethality due to paralysis, preventing eclosion of the adult from the pupal case. According to mendelian inheritance, the theoretical ratio of progenies with 30 HRE expressions from the above crossing is 50%. A total of 100 adult flies are collected in each group.

Neuron survival assay and ASO treatment

The neuron survival assay was initiated on Day 14. At this juncture, the iMNs were maintained in N3 media that did not contain neurotrophic factors and RepSox. Baseline images were taken using the Molecular Devices Image Express prior to the addition of ASOs.

The following day iMNS were treated (a single time) with 9 μM of negative control ASO, p53 ASO-1, and p53 ASO-2 for 72 hours. The ASOs were synthesized by Integrated DNA Technologies which contained Gapmer modification for increased stability and binding affinity. Longitudinal tracking of Hb9::RFP iMNs was performed by imaging the plates every 2 days and iMNs were manually counted using SVCell 3.0 (DRVision Technologies). Neurons were scored as dead when their soma were no longer visible.

Lentiviral production

HEK293T (ATCC) cells were used to package lentiviral particles according to standard protocols with third-generation packaging plasmids (pMDlg-pRRE, pRSV-ReV, pMD2.0; Addgene). Lentiviral backbone and packaging plasmids were transfected into HEK293T cells using Lipofectamine 3000 and Lentivirus-containing medium was harvested after 48 h. Viral supernatant was collected and filtered through a 0.45 μm filter to remove cellular debris. The virus was concentrated using Lenti-X concentrator (Clontech) and re-suspended in Neurobasal/B27. Lentivirus was added to cortical neurons 3 days after plating. For overexpression experiments, TDP-43 ORF from the human ORFeome collection, GFP or $(PR)_{50}$-FLAG constructs were cloned into a third-generation lentiviral vector for expression of the transgenes under the control of the neuron-specific human synapsin 1 promoter (SYN).

To knockdown p53 in iPSC-derived neurons, we generated lentiviral particles using the addgene plasmid 25636, pLKO-p53-shRNA-427. Then, we transduced 2-month-old iPSC-derived motor neurons from two *C9orf72* carriers, for two additional weeks to perform comet assay.

Comet assay

The comet assay was performed in iPSC-derived motor neurons from 2 independently generated C9orf72 ALS/FTD patients and their respective isogenic controls as described in (Lopez-Gonzalez et al., 2016; Olive and Banáth, 2006). Briefly, motor neuron cultures were dissociated mechanically and enzymatically to obtain a single-cell suspension. Cell suspensions were mixed with a 1% low-gelling 2 hydroxyethyl agarose solution (Sigma-Aldrich) and placed on glass slides and allowed to gel. Then slides were gently submerged in lysis solution and left overnight at 4°C. Slides were transferred to an electrophoresis solution, run at 0.6 V/cm for 25 min, removed, and submerged in rinse buffer for 30 min at room temperature. Afterward, the slides were incubated with 2.5 μg/ml SYBR Safe (Invitrogen) for 20 min and washed with distilled water. For each experimental condition, 20 cells were analyzed with ImageJ software, and scored based on tail length and percentage of DNA in the tail.

siRNA treatment

siRNA oligonucleotide sequences were used to target p53, p63, p73 and *Puma* (Dharmacon, ONTARGETplus SMARTpool). For negative control, a nontarget sequence was used (Dharmacon, ON-TARGETplus Non-Targeting Pool, D-001810). Cortical neurons dissociated cells were transfected with siRNA 3 days after plating, using the protocol supplied with DharmaFECT 4 (Dharmacon, T-2004-03) and performed as previously described before (Maor-Nof et al., 2013) with minor modifications. Briefly, siRNA and the transfection reagent were each diluted separately into NB medium without serum and antibiotics for 5 min; then, the siRNA was added to the medium with the transfection reagent. After an additional 20 min incubation, the transfection reagent siRNA complex was added to the dissociated cells and grown in NB medium without serum and antibiotics. 16h later, the transfection reagent was removed by replacing the medium with a complete medium and the neurons were cultured for an additional 48 hr. Lentivirus transduction was performed after. The final concentration of the siRNA was 0.1 mM. The level of the target protein *Puma*, reduced by its specific siRNA treatment, was evaluated by western blot analysis.

Immunoblotting

Primary cortical neurons were washed with ice-cold PBS prior to lysis. Cells were lysed in 1 × RIPA lysis supplemented with 1 × Halt protease and phosphatase Inhibitor Cocktail (Thermo Fisher Scientific cat# 78429, 78426) and incubated for 30 min on ice. Crude RIPA lysates were centrifuged at 14,000 g for 15 min at 4°C to remove cellular debris. The remaining supernatant was transferred to a new tube and quantified with a Pierce BCA protein assay (Thermo Fisher Scientific cat# 23225). Cell lysates were mixed with 4 × NuPage LDS loading buffer and beta-mercaptoethanol and incubated for 10 min at 95°C. Equal amounts of protein were subjected to SDS–PAGE, transferred to nitrocellulose membranes. Membranes were blocked with 5% BSA in tris-buffered saline with 0.1% Tween (TBST) at RT for 1h and treated over night at 4°C with primary antibodies. Following incubation overnight, horseradish peroxidase-conjugated secondary antibodies and an ECL kit (GE Healthcare/Amersham Pharmacia Biotech) were used to detect protein signals. Multiple exposures were taken to select images within the dynamic range of the film (GE Healthcare Amersham Hyperfilm ECL). Protein bands were quantified using Fiji software (NIH). For the fluorescent western images, after primary antibody incubation, the membranes were washed with PBST and incubated with IRDye anti-rabbit or anti-mouse secondary antibodies (1:5000, LI-COR Biosciences) and images were acquired with the Odyssey CLx imaging system.

Immunocytochemistry

Primary cortical neurons were grown on poly-L-lysine-coated glass coverslips [0.1% (wt/vol)] in standard multi-well cell culture plates and were stained through standard immunocytochemistry techniques. Briefly, cells were fixed with 4% formaldehyde and 15% sucrose for 1h at RT, rinsed 3 times with PBS, blocked with 1% BSA and permeabilized with 0.3% Triton X-100 for 1h at RT. After overnight primary antibody incubation, cells were rinsed 3 × with PBS. Cells were incubated with fluorescently labeled secondary

antibodies for 1h at room temperature. Coverslips were mounted with Prolong Diamond Antifade mount with DAPI (Thermo Fisher Scientific). Images were acquired with a Leica DMI6000B inverted fluorescence microscope.

ATAC-seq

Primary cortical neurons treated for 20, 40 and 60h with either GFP, $(PR)_{50}$, TDP-43 or untreated, were pretreated with 200 U/ml DNase (Worthington) for 30 min at 37°C to remove free-floating DNA and to digest DNA from dead cells. This medium was then washed out, and the cells were washed in cold PBS four times. To avoid neuronal cell death that is associated with trypsinization, neurons were directly lysed in 1ml of cold ATAC-seq resuspension buffer (RSB; 10mM Tris-HCl pH 7.4, 10mM NaCl, and 3mM $MgCl_2$ in water, containing 0.1% NP40, 0.1% Tween-20, and 0.01% digitonin) on ice for 10 min. After lysis cells nuclei were collected and counted, 50,000 viable cells were centrifuged at 500xg for 5 min in a pre-chilled (4°C) fixed-angle centrifuge. After centrifugation, supernatant was carefully aspirated, with two pipetting steps; The remaining 100 μL of supernatant was carefully aspirated by pipetting with a P200 pipette tip to avoid the cell pellet. Cell pellets were then resuspended in 1 mL of ATAC-seq RSB containing 0.1% Tween-20 (without NP40 or digitonin), and the tubes were inverted to mix. Nuclei were then centrifuged for 10 min at 500 RCF in a pre-chilled (4°C) fixed-angle centrifuge. Supernatant was carefully removed with two pipetting steps, as described before, and nuclei were resuspended in 50 μL of transposition mix (25 μL 2 × TD buffer (20 mM Tris-HCl pH 7.6, 10 mM $MgCl_2$, 20% Dimethyl Formamide), 2.5 μL transposase (100 nM final), 16.5 μL PBS, 0.5 μL 1% digitonin, 0.5 μL 10% Tween-20, and 5 μL water) by pipetting up and down six times. Transposition reactions were incubated at 37°C for 30 min in a thermomixer with shaking at 1,000 rpm Reactions were cleaned up with Zymo DNA Clean and Concentrator columns.

The complete eluate underwent PCR, as follows. After initial extension, 5 cycles of pre-amplification using indexed primers (Buenrostro et al., 2015) and NEB Next High-Fidelity 2X PCR Master Mix (NEB) were conducted, before the number of additional cycles was assessed by quantitative PCR using SYBR Green. Typically, 7-9 additional cycles were run. The final library was purified using a MinElute PCR kit (QIAGEN) and quantified using a Qubit dsDNA HS Assay kit (Invitrogen) and a High Sensitivity DNA chip run on a Bioanalyzer 2100 system (Agilent). All libraries were sequenced using 75bp Nextseq High Output Cartridge kits and a Nextseq 500 sequencer (Illumina).

ATAC-seq analysis

ATAC-seq libraries were trimmed to remove illumina adapters using SeqPurge (Sturm et al., 2016) and mapped to the mouse reference genome (mm9) using Bowtie2 v2.3.4.1 with the following parameters "–very-sensitive -X 2000–no-mixed–no-discordant" (Langmead and Salzberg, 2012). PCR duplicate reads were removed using Picard MarkDuplicates v2.17.10 (http://broadinstitute.github.io/picard). The reads were filtered using samtools v1.5 for a minimum mapping quality of 10 and only properly paired reads were retained. Additionally, any reads aligning to the mitochondrial chromosome were removed. Peaks were called subsequently on each sample using macs2 v2.1.1.20160309 with the following parameters "–keep-dup all -f –nomodel –call_summits -q 0.05" (Zhang et al., 2008). Peaks were filtered against the ENCODE blacklist (https://sites.google.com/site/anshulkundaje/projects/blacklists). Combined peaks set with fixed width (500bp wide) was generated by first running IDR 2.0.4 on the replicates of each sample to find peaks that are consistent between replicates, we then merged peaks from all samples by expanding all summits to 500bp, in cases where multiple peaks merged together we split into most possible non overlapping peaks going from strongest summits to weakest. Number of fragments within peaks were counted using featureCounts (Liao et al., 2014).

To determine differential peaks, the raw counts matrix was used as input into DESeq2 (Love et al., 2014) and edgeR (Nikolayeva and Robinson, 2014) both in a pairwise way between all samples and between treatments (PR/TDP) against GFP (Figures S2G–S2L). We then took top 3960 differential peaks and clustered the log2 (CPM) values (obtained using edgeR with library size normalization) using K-means++ (K = 12) (https://github.com/tanaylab/tglkmeans).

We used motifMatcher (part of chromVar package) to call TF binding sites within each of the 3960 peaks, using hypergeometric test we computed the enrichment of each TF within each cluster compared to the other 3960 differential peaks. To compute TF motif deviations, chromVAR was used in R with raw counts in all peaks and then the top 100 variable TF motifs were determined using variability scores (Schep et al., 2017).

To generate motif match matrices, motifs from the curated, high-confidence JASPAR2016 vertebrate core database were obtained. We called significant motif matches in peaks, or subsets of peaks, using JASPAR motif position weight matrices and the function "matchMotifs" from the "motifmatchr" and "chromVAR" packages v1.8.0 (https://bioconductor.org/packages/release/bioc/html/chromVAR.html), resulting in a binary peaks-by-matches matrix. To compute enrichments, we defined foreground and background peak sets according to the specific question addressed, then performed a two-sided Fisher's Exact test for the over or under representation of each motif in the foreground set. For K-means cluster motif enrichments, we aggregated all peaks from a given K-means cluster and tallied the total number of matches for each motif in the cluster, and we used all of the other clusters as the background.

RNA-seq

RNA was isolated from primary neurons treated for 20, 40 and 60h with either GFP, $(PR)_{50}$, TDP-43 or untreated. To obtain RNA from the same neurons that were used for ATAC-seq, we performed sequential lysis. Neurons were first lysed in ATAC-seq resuspension RSB buffer, followed by sequential RNA extraction and isolation in RLT buffer of the QIAGEN RNeasy Plus Micro Kit (QIAGEN),

according to the manufacturer's protocol. In brief, cells were lysed, homogenized, and loaded on a genomic DNA (gDNA) eliminator column. After removal of genomic DNA, RNA was purified using RNeasy spin columns. RNA quantity and purity were determined by optical density measurements of OD260/280 and OD230/260 using a NanoDrop spectrophotometer. Structural integrity of the total RNA was assessed using a 2200 TapeStation Instrument with RNA ScreenTapes (Agilent Technologies, Santa Clara, CA). mRNA libraries were prepared using a SureSelect Strand-Specific RNA Library Preparation kit for Illumina (G9691B) on an Agilent Bravo Automated Liquid Handling Platform, following the manufacturer's protocol. Libraries were sequenced on an Illumina HiSeq 4000.

RNA-seq analysis

Alignment of RNA-sequencing reads to the mouse mm10 transcriptome was performed using STAR v2.7.3a (Dobin et al., 2013) following ENCODE standard options, read counts were generated using RSEM v1.3.1, and differential expression analysis was performed in R v3.6.1 using the DESeq2 package v1.38.0 (Love et al., 2014), detailed pipeline v2.0.1 and options available on https://github.com/emc2cube/Bioinformatics/ and the Visualization Pipeline for RNA-seq (VIPER)(Cornwell et al., 2018). We took 6109 differentially expressed genes (DEG) between all samples and clustered the Z-score changes using K-means++ (K = 6) (https://github.com/tanaylab/tglkmeans). For each cluster we performed KEGG pathway enrichment between the genes found in the cluster to all DEG using gProfiler (https://biit.cs.ut.ee/gprofiler).

Next, we generated a co-expression network for samples from 40h and 60h using the WGCNA package in R (Langfelder and Horvath, 2008). We used a soft threshold power of 12 to generate a topological overlap matrix (TOM). The TOM was clustered hierarchically using average linkage hierarchical clustering (using 1 – TOM as a dissimilarity measure). The topological overlap dendrogram was used to define modules using the cutreeHybrid() function with parameters: minimum module size = 100, deep split = 4, merge threshold = 0.1, and negative pamStage. To identify modules associated with time or treatment, we fit four different linear model contrasts for the eigengenes of each module: 60h versus 40h, GFP samples versus Control samples, $(PR)_{50}$ samples versus GFP and Control samples, and TDP-43 samples versus GFP and Control samples. For enrichment analysis, we downloaded p53 target genes from KEGG. We used logistic regression to test whether each module was enriched with p53 target genes. For gene ontology enrichments, we used the g:Profiler package in R (Reimand et al., 2007) with parameters: correction_method = fdr, max_set_size = 1000, and hier_filtering = moderate. We performed ordered queries with genes ordered by connectivity to the module eigengene (kME) for each co-expression module.

CRISPR-Cas9 screens in G401 cells

The 10-sgRNA per gene CRISPR/Cas9 epigenetic sublibrary was synthesized, cloned, and infected into Cas9 expressing G401 cells as previously described (Kramer et al., 2018; Morgens et al., 2017). Briefly, 100 million G401 cells stably expressing SFFV-Cas9-BFP were infected with the 10 guide/gene transcription factor sgRNA library at a MOI < 0.4. Infected cells underwent puromycin selection (1μg/mL) for 5 days after which point puromycin was removed. After selection, sgRNA infection was measured by immunofluorescence to confirm that > 90% of cells were mCherry+. Cells were maintained for three weeks at 1000 × coverage (~1000 cells containing each sgRNA) at a concentration of 500,000 cells/mL for the duration of each screen. Cells were split into two conditions: one control group that remained untreated, and one group that was treated with the synthetic $(PR)_{20}$ at 4 μM. This treatment occurred four times over three weeks, allowing for cells to recover to ~90% viability after each round of treatment. At the end of each screen genomic DNA was extracted for all screen populations separately according to the protocol included with QIAGEN Blood Maxi Kit and deep sequencing on an Illumina Nextseq 500 was used to monitor library composition. Guide composition between PR treated conditions was compared to the untreated condition using casTLE (Morgens et al., 2016) version 1.0. Briefly, the enrichment of individual guides was calculated as log ratios between treated and untreated conditions, and gene-level effects were calculated from ten guides targeting each gene. A confidence score was then derived as a log-likelihood ratio describing the significance of the gene-level effect. P values were then calculated by permutating the targeting guides as previously described (Morgens et al., 2016).

QUANTIFICATION AND STATISTICAL ANALYSIS

All images were quantified using the following computerized algorithms tailored to each paradigm and written in MATLAB or C++.

Axonal quantification *in vitro*

The images of cortical neurons, immuno-stained for β-tubulin, were binarized such that pixels corresponding to axons converted to white while all other regions converted to black. To perform this binarization and differentiate between axons and background in the images, a localized Otsu threshold was used. The Otsu algorithm searches for a threshold that minimizes the variance sum of two or more populations in an image (Otsu, 1979).This gives an exact threshold below which all pixels are considered background. This threshold was then applied to count the number of pixels corresponding to axons in each figure, which serves as the MTs stability index. A punctuated formation of MTs was evident from the cortical explants' staining; these spots occupy only the higher gray levels in the image and appeared mostly in the $(PR)_{50}$ and TDP-43 treated, and not in their corresponding GFP treated and the untreated neurons. The MT depolymerization index was defined as the ratio of depolymerized axon pixel number to intact axon pixel number. To detect the depolymerized axons, we used an algorithm for counting all the pixels above a certain threshold. To find this threshold, we calculated the probability density function (PDF) of the sum-controlled experiments (untreated neurons), from which the

cumulative probability density function (CDF) was extracted. The threshold was set as the value above which there were almost no pixels (less than 0.1%). More than six wells were analyzed for each experimental condition.

Number of GFP, p53 positive cells and their colocalization

The number of positive p53 cells from mouse tissue was identified using a specific p53 antibody (Figure S4A) that stained in red cells expressing p53. p53 expressed cells were distinguished from the background using the statistics of the background with a 4σ threshold. The statistics were calculated using the robust statistics technique, which is less prone to errors from outliers. The result was a binarized image were the p53 expressing cells were "on." The image was subjected to several morphological operations intended to remove noise and fill gaps. Connected components analysis was used to identify the individual connected cells and count them.

The number of positive GFP expressing cells was identified using the GFP from the construct GFP-$(PR)_{50}$ in the green channel. GFP expressed cells were distinguished using the same algorithms as for p53. The binary images of p53 and GFP were co-localized by applying a logical "AND" operator between the two images. The resulting binary image shows only the locations where both p53 and GFP expressed cells were found in the same coordinates. Connected components analysis was used to identify the individual connected cells and count them.

Axonal degeneration index

Following $(PR)_{50}$ and TDP-43 treatments, phase microscopy images of live cells revealed fragmented axons of cortical neurons. The axonal integrity index is defined as the slope of the rate of axon degradation. Images with intact axons were characterized by a higher number than those with fragmented axons. The algorithm starts by identifying the pixels in the image classified as the cell body. Those pixels will later be used as a mask and will not contribute to our result. The cell body is easily identified in the images as extremely bright/dark saturated pixels that can be identified using a double threshold. Following that we distinguished between the axons and the image background. This can be achieved via robust statistics of the image's gray levels. Once axonal pixels are identified, morphological operations are applied to the binary image to clean it up. The cell body mask is applied, and its pixels are removed. Connected component analysis is used on the resulting binary image to find all the axons and to create the quantification number of the amount of axonal material. More than three wells were analyzed per each experimental condition.

Statistical methods

Analyses were performed using R, Microsoft Excel or Prism 8 (GraphPad), and graphs were plotted using Microsoft Excel or Prism 8. Survival curves were compared using the survdiff function in the survival R package, which performs a log-rank test, and effect sizes are reported as the hazard ratios given by the coxph function, which fits a Cox proportional hazards model. For comparisons among different genotypes or treatment groups, pairwise analyses were conducted by unpaired t test for two groups and one-way ANOVA were used when comparing more than two groups. Data represent mean ± SEM unless otherwise noted.

Significance is indicated at the figure legends.

Supplemental Figures

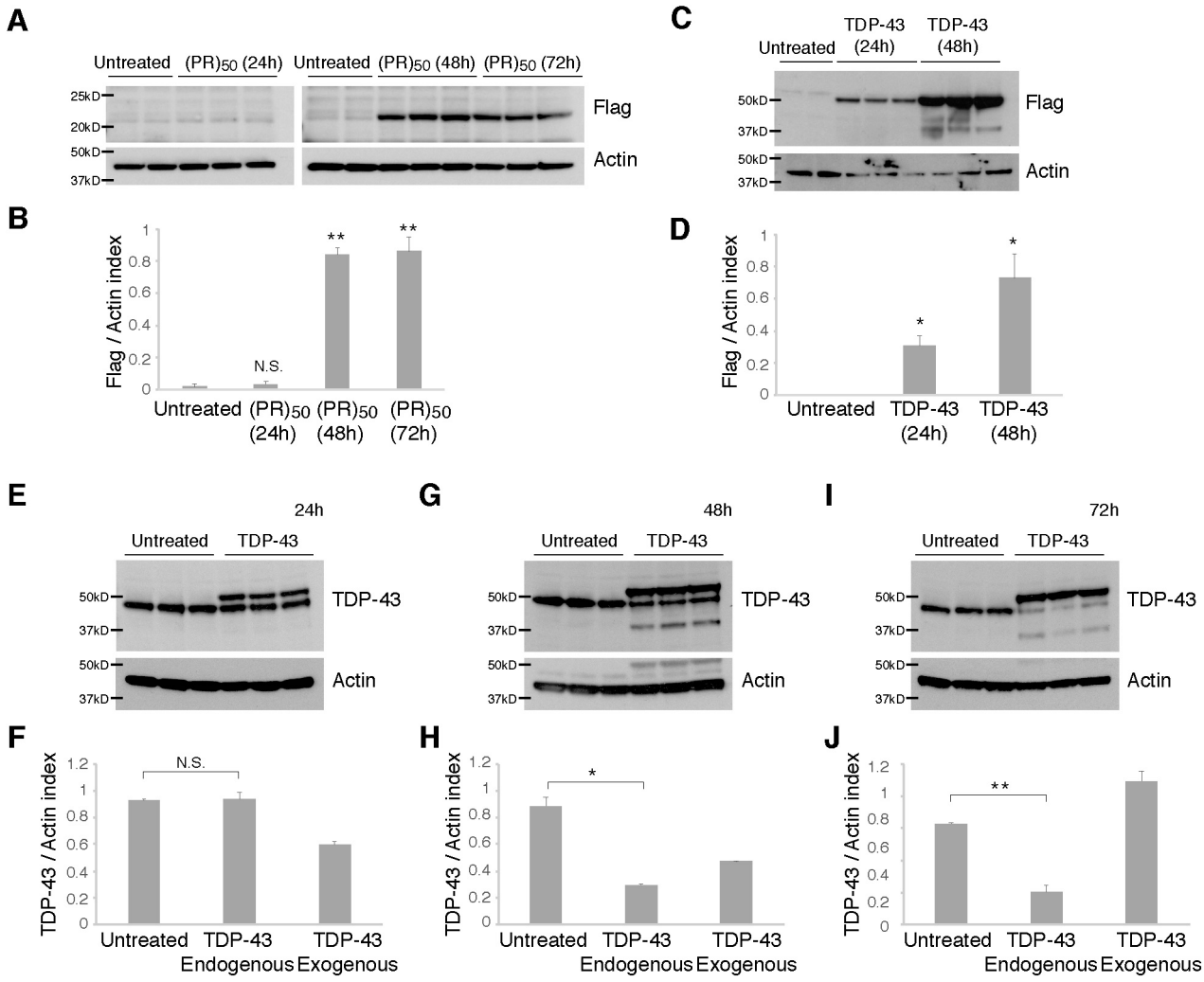

Figure S1. Cortical neurons expressing C9orf72 $(PR)_{50}$ or TDP-43, related to Figure 1

(A–J) Cortical WT primary neurons were cultured for 3 days and treated with either *C9orf72* $(PR)_{50}$ or TDP-43 for additional 24h, 48h or 72h or left untreated. $(PR)_{50}$ levels were elevated at both 48h and 72h of $(PR)_{50}$ treated neurons, as detected using the anti-Flag antibody (A-B). TDP-43 levels were elevated at 24h (C-D and E-F), 48h (C-D and G-H) and 72h (I-J) of TDP-43 treated neurons, as detected using the anti-Flag antibody (C) and a specific anti TDP-43 (E, G and I) antibody. Quantitation of $(PR)_{50}$ and TDP-43 was determined by immunoblots and normalized to actin (B, D, F, H and J). Graphs show mean ± SEM (t test; *$p < 0.05$, **$p < 0.01$, N.S. not significant).

A

Name	Total	Post chrM	Post Filter	Post Dedup	chrM reads	% chrM	Duplicate reads	% Duplicated reads	TSS Enrichment
GFP_20h1	32,422,402	28,379,646	23,269,040	22,172,906	4,042,756	12.47%	1,096,134	3.38%	12.1
GFP_20h2	42,393,682	36,289,389	29,224,144	27,565,608	6,104,293	14.40%	1,658,536	3.91%	11.7
Untreated_20h1	36,680,376	33,919,244	29,289,654	27,892,302	2,761,132	7.53%	1,397,352	3.80%	8
Untreated_20h2	23,441,726	20,396,926	17,930,160	17,030,556	3,044,800	12.99%	899,604	3.84%	10.6
PR(50)_20h1	41,673,772	34,817,563	28,981,956	27,453,684	6,856,209	16.45%	1,528,272	3.67%	11.5
PR(50)_20h2	31,846,832	26,232,084	21,690,202	20,791,366	5,614,748	17.63%	898,836	2.82%	11.2
TDP-43_20h1	35,250,632	29,649,936	24,158,362	22,893,798	5,600,696	15.89%	1,264,564	3.59%	11.7
TDP-43_20h2	28,018,924	23,775,220	19,610,064	18,655,946	4,243,704	15.15%	954,118	3.41%	11.8
GFP_40h1	33,190,454	28,005,351	23,390,442	22,449,490	5,185,103	15.62%	940,952	2.83%	10
GFP_40h2	48,968,358	41,191,163	34,272,228	32,623,232	7,777,195	15.88%	1,648,996	3.37%	9.8
Untreated_40h1	27,662,876	24,671,190	21,960,582	20,922,568	2,991,686	10.81%	1,038,014	3.75%	10.1
Untreated_40h2	31,327,572	27,939,095	24,937,970	23,730,646	3,388,477	10.82%	1,207,324	3.85%	10
PR(50)_40h1	39,854,180	32,565,947	27,720,202	26,444,134	7,288,233	18.29%	1,276,068	3.20%	9.9
PR(50)_40h2	29,104,074	23,223,313	19,540,550	18,786,502	5,880,761	20.21%	754,048	2.59%	9.6
TDP-43_40h1	32,202,692	26,860,341	22,773,528	21,848,914	5,342,351	16.59%	924,614	2.87%	9.7
TDP-43_40h2	33,186,088	27,497,152	23,199,330	22,256,178	5,688,936	17.14%	943,152	2.84%	9.6
GFP_60h1	34,912,342	30,251,748	25,947,606	24,683,686	4,660,594	13.35%	1,263,920	3.62%	9.7
GFP_60h2	36,972,042	32,425,437	27,995,456	26,538,840	4,546,605	12.30%	1,456,616	3.94%	10.1
Untreated_60h1	34,220,894	31,170,830	28,479,160	26,585,722	3,050,064	8.91%	1,893,438	5.53%	10.9
Untreated_60h2	33,027,090	30,124,936	27,515,340	25,729,096	2,902,154	8.79%	1,786,244	5.41%	10.1
PR(50)_60h1	38,649,990	28,177,543	23,333,818	22,250,522	10,472,447	27.10%	1,083,296	2.80%	9.9
PR(50)_60h2	29,113,084	20,902,601	17,228,242	16,534,764	8,210,483	28.20%	693,478	2.38%	9.6
TDP-43_60h1	49,457,108	34,529,717	27,854,684	26,437,674	14,927,391	30.18%	1,417,010	2.87%	10.3
TDP-43_60h2	53,315,602	38,262,667	31,184,424	29,568,990	15,052,935	28.23%	1,615,434	3.03%	10.2

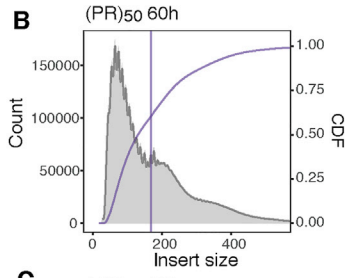

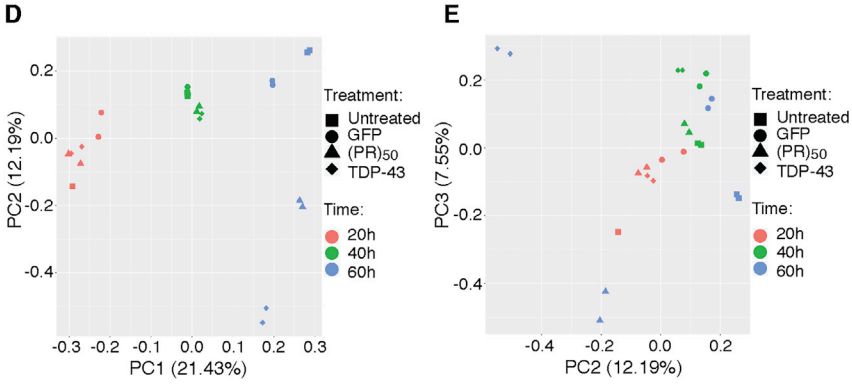

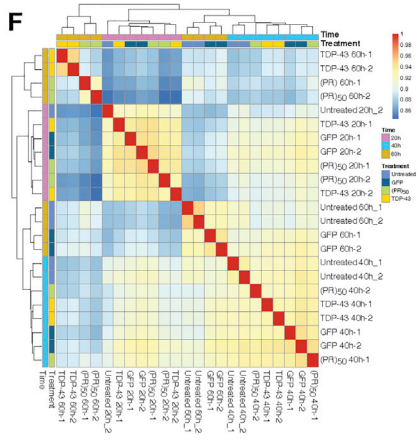

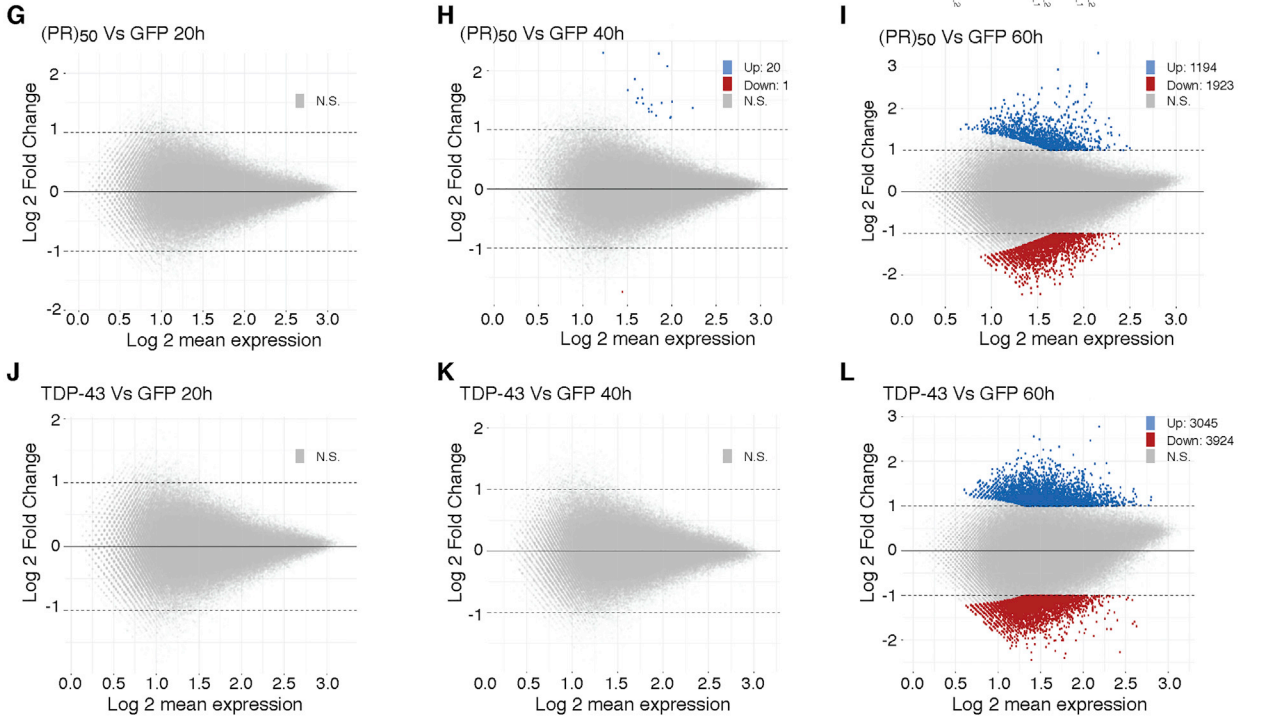

(legend on next page)

Figure S2. ATAC-seq analysis of cortical neurons treated with GFP, C9orf72 $(PR)_{50}$, or TDP-43, related to Figure 1

(A) Table with all the ATAC-seq samples used in this study.

(B and C) Quality check for the ATACseq samples presented here is one example, $(PR)_{50}$ at 60h. Insert size distribution (B) and transcription start site enrichment around Refseq annotated genes(C).

(D and E) PCA analysis of all merged peaks provides an overall visualization of the data, emphasizing the variation and brings out strong patterns. PC1 versus PC2 show that PC1 (21% of the variability) is associated with time, while PC2 (12% of the variability) is associated with the different treatments (D). PC2 Vs PC3 emphasizes the variation in between the different treatments over time (E).

(F) Pearson correlation between the counts of all merged peaks.

(G–I) MA Plots of $(PR)_{50}$ versus GFP treated neurons, from 20, 40 and 60h post treatment. Small changes in ATAC-seq start appearing at 40h but the majority of changes are around 60h post treatment.

(J–L) MA Plots of TDP-43 versus GFP treated neurons, from 20, 40 and 60h post treatment.

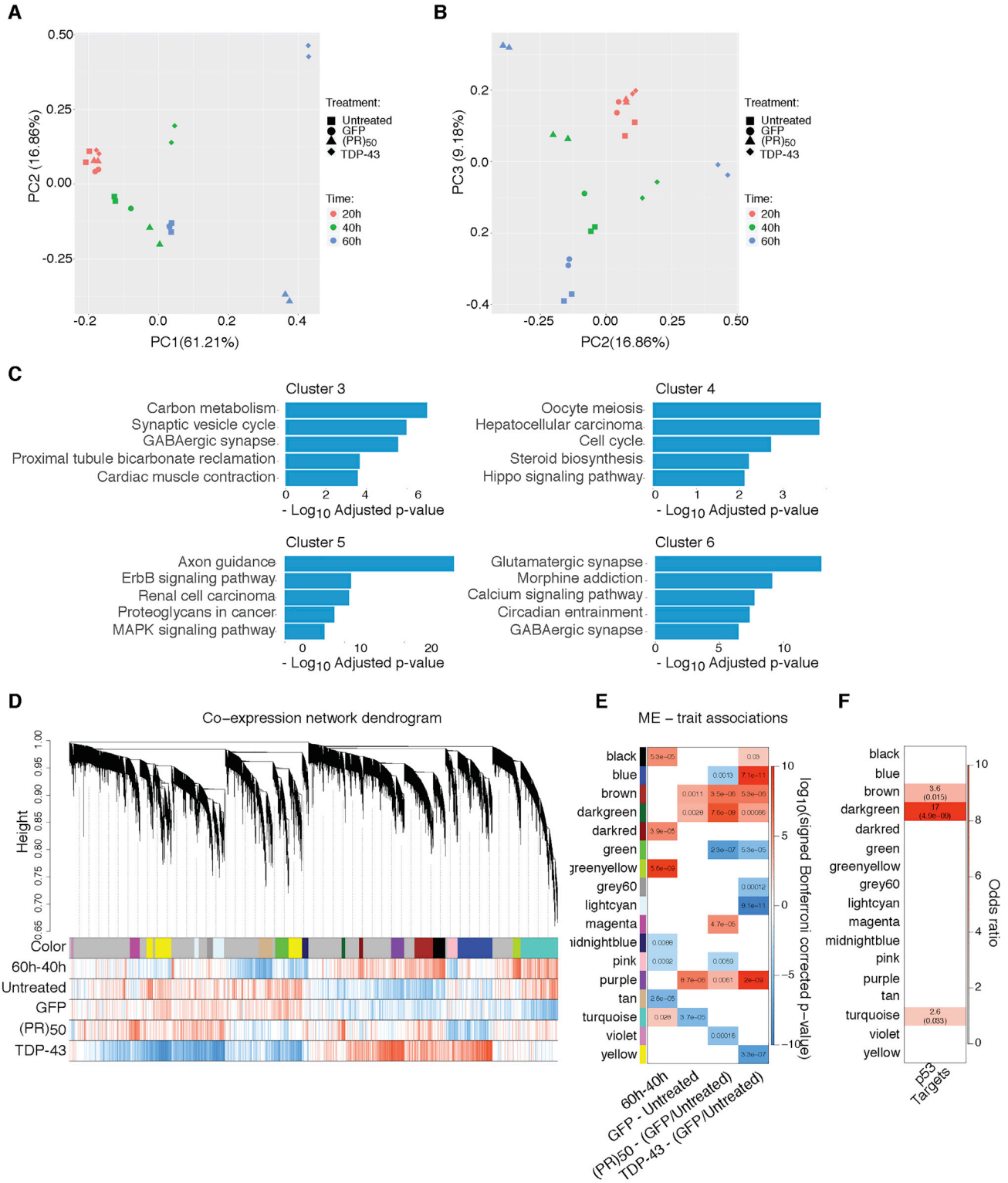

Figure S3. RNA-seq analysis of cortical neurons treated with GFP, *C9orf72* $(PR)_{50}$, or TDP-43, related to Figure 2

(A and B) PCA analysis of all transcripts is used to visualize the data and show an overall view of the data. (A)PC1 versus PC2 show that PC1 (61.21% of the variability) is associated with time, while PC2 (16.86% of the variability) is associated with the different treatments. (B) PC2 Vs PC3 emphasizes the variation in between the different treatments over time.

(legend continued on next page)

(C) KEGG pathway gene ontology enrichment of clusters 3-6 of the K-means clustering analysis (Figure 2C). FDR corrected p value.
(D–F) Average linkage hierarchical clustering using the topological overlap metric for co-expression dissimilarity. (D) Modules were identified from this dendrogram. Correlations for each gene to covariates are delineated below the dendrogram (blue, negative; red, positive). Modules are labeled with colors. The gray module represents genes that are not co-expressed and was not evaluated in further comparisons. (E) Module-trait associations as computed by a linear model with four contrasts: 60h versus 40h, GFP versus Control, $(PR)_{50}$ versus GFP + Control, and TDP-43 versus GFP + Control. Only p values with a Bonferroni-corrected value < 0.05 are shown. (F) Enrichments for all of the co-expression modules with a list of p53 target genes. FDR corrected p values are shown in parentheses.

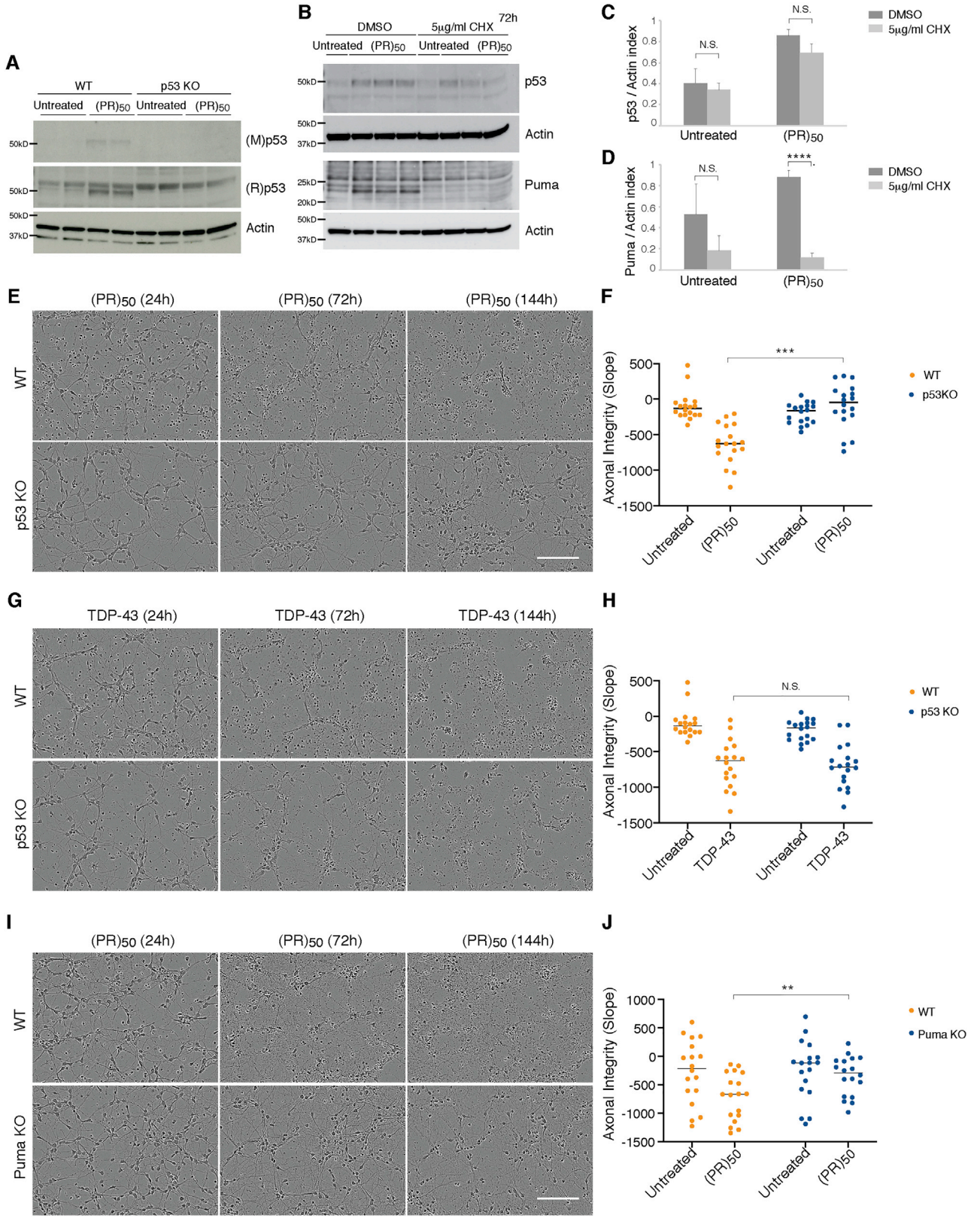

(legend on next page)

Figure S4. p53 ablation protects neurons from $(PR)_{50}$ toxicity, but not from TDP-43, related to Figures 3 and 7

(A) Two specific p53 antibodies were detected after $(PR)_{50}$ treated WT neurons while absent in the p53 KO neurons.

(B–D) Cortical neurons from p53 KO embryos or their WT littermates were cultured for 3 days and either treated with $(PR)_{50}$ or left untreated for 48h. 5 mg/ml cycloheximide or DMSO for control were added for additional 24h, followed by lysis and immunoblotting. Elevated p53 levels were detected in the presence of the protein inhibitor cycloheximide (B and C), while for puma this increase was completely blocked (B and D). Quantitation of p53 and puma was determined by immunoblots and normalized to actin (C and D). Graphs show mean ± SEM (t test; ****$p < 0.0001$, N.S. not significant).

(E–H) Cortical neurons from p53 KO embryos or their WT littermates were cultured for 3 days and either left untreated or treated with $(PR)_{50}$ (E) or TDP-43 (G) and monitored using live-cell imaging. WT cortical neurons were fragmented after $(PR)_{50}$ and TDP-43. The p53 KO cortical neurons and axons were completely protected from any degradation after $(PR)_{50}$ (E) but not TDP-43 (G) treatment. Axonal integrity (mean index) was calculated by measuring the slope of the degradation rate for each genotype and condition (F and H), as described in the Supplemental Experimental Procedures (t test; ***$p < 0.001$, N.S. not significant). Scale bars, 150 μm.

(I and J) Puma ablation protects neurons from (PR)50 toxicity. Cortical neurons from *Puma* KO embryos or their WT littermates were cultured for 3 days and either left untreated or treated with $(PR)_{50}$ and monitored using live-cell imaging (I). WT cortical neurons were fragmented after $(PR)_{50}$. The *Puma* KO cortical neurons and axons were protected for the duration of 120h after $(PR)_{50}$ treatment. Axonal integrity (mean index) was calculated by measuring the slope of the degradation rate for each genotype and condition (J), as described in STAR methods (t test; **$p < 0.01$). Scale bar, 150 μm.

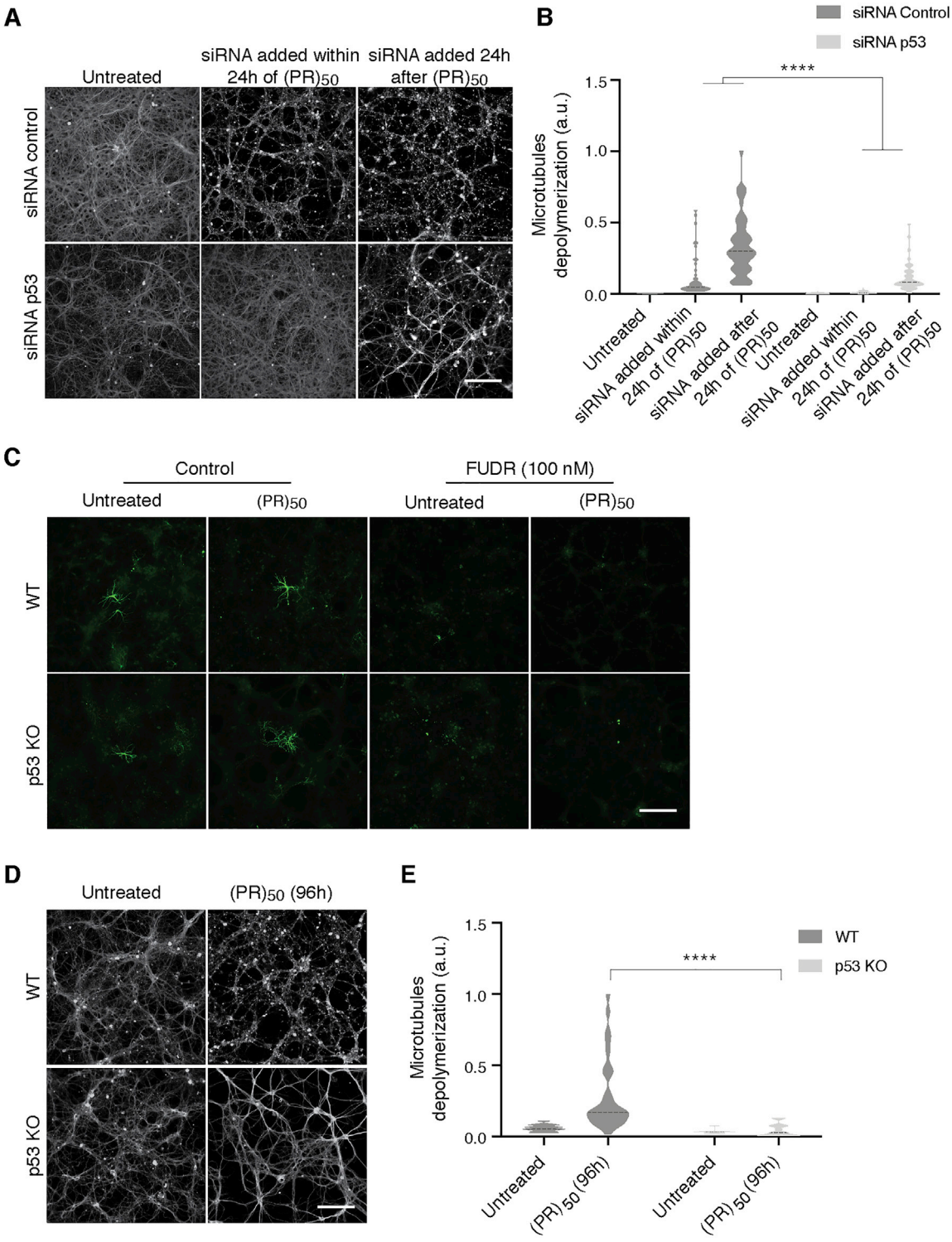

Figure S5. p53 ablation protects neurons from $(PR)_{50}$ toxicity in the absence of glial cells, related to Figure 4

(A and B) WT cortical neurons were cultured for 3 days and treated with $(PR)_{50}$ for additional 72h. Neurons were then either treated within the first 24h or after 24h of $(PR)_{50}$ induction with siRNA against *p53* or non-targeting control and immunostained for tubulin βIII. *p53* siRNA addition within the first 24h of $(PR)_{50}$ treatment protected against axonal degeneration (A). The extent of microtubule depolymerization (mean index) was calculated for each condition (B), as described in STAR methods (t test; ****$p < 0.0001$). Scale bar, 100 μm.

(legend continued on next page)

(C–E) Cortical neurons from p53 KO embryos or their WT littermates were cultured for one day and 100nM FUdR was added for 8h. Following this treatment, no glial cells were present as detected by GFAP immunostainings (C). Axonal microtubules (MTs) of the WT cortical neurons were depolymerized and degraded after $(PR)_{50}$. The p53 KO cortical neurons and axons were completely protected from any degradation after $(PR)_{50}$ treatment (D). The extent of microtubule depolymerization (mean index) was calculated for each genotype and condition (E), as described in STAR methods (t test; ****$p < 0.0001$, N.S. not significant). Scale bar, 100 μm.

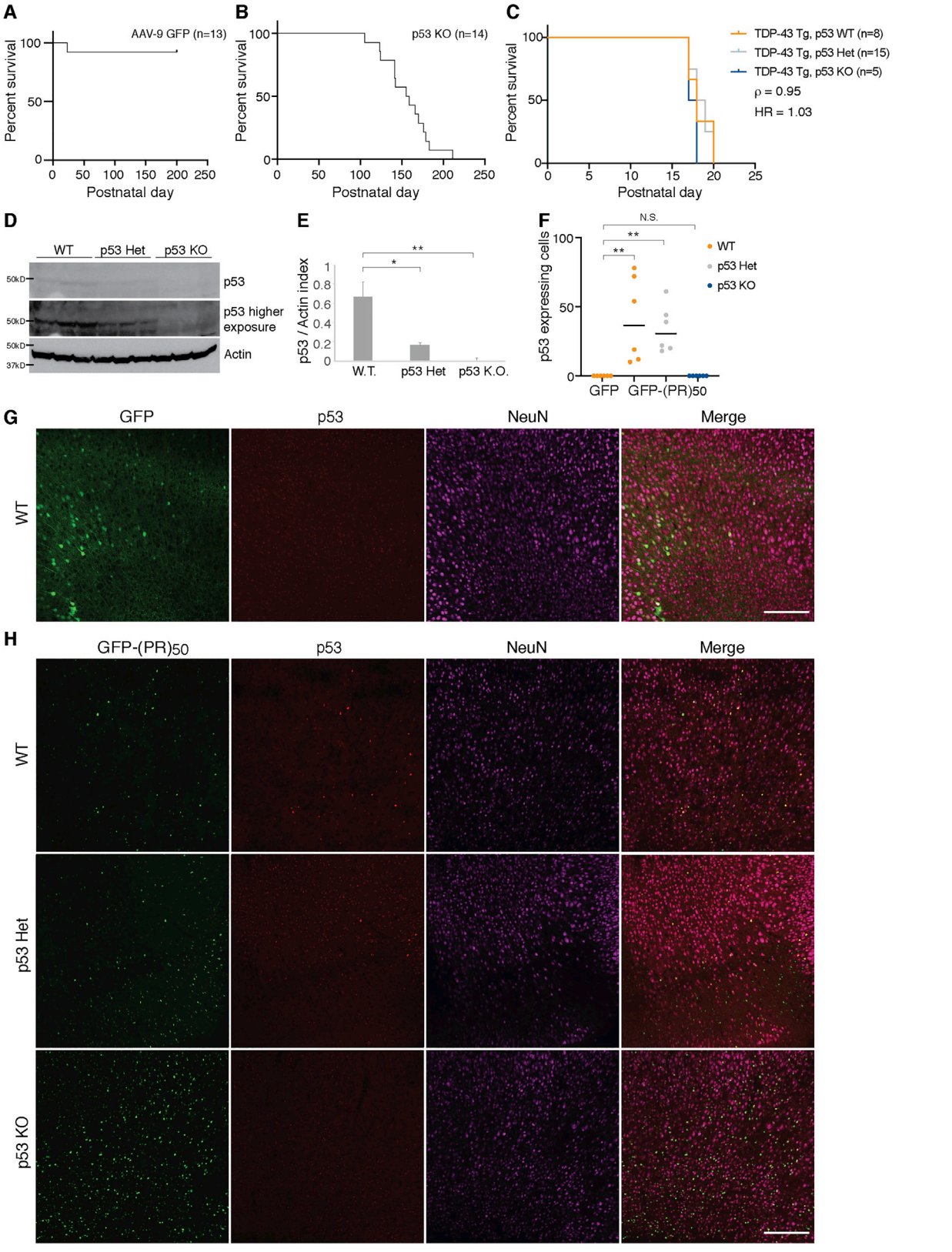

(legend on next page)

Figure S6. p53 is activated and colocalized with $(PR)_{50}$ in brains of *C9orf72* $(PR)_{50}$ mice, related to Figure 5

(A) Newborn pups from p53 heterozygous x heterozygous crosses were injected with GFP.

(B) Viability of p53 KO mice (n = 14) monitored for a total of 211 days.

(C) Kaplan-Meier survival curves comparing survival of WT (n = 8), p53 heterozygous (n = 15) and p53 KO (n = 5) TDP-43 transgenic mice. Curves were compared by log-rank test and effect size was estimated by a Cox proportional hazards model (HR).

(D and E) Nucleocytoplasmic fractioning of mouse brain tissue. p53 were detected in WT nuclear fraction, reduced in p53 heterozygous and ablated in p53 KO mice (D). Samples were collected at P22. Quantitation of p53 was determined by immunoblots and normalized to actin (E). Graphs show mean ± SEM (one-way ANOVA; $*p < 0.05$, $**p < 0.01$).

(F–H) Immunofluorescence staining of WT and p53 KO 3-weeks-old mice show no activation in GFP expressing cells (G), whereas strong p53 activation in the cortex (H) of WT GFP-$(PR)_{50}$ expressing cells. Three mice per each genotype and condition were quantified (F) as described in the Supplemental Experimental Procedures and the values of p53-expressing cells are plotted (one-way ANOVA; $**p < 0.01$, N.S. not significant). Scale bars, 200 μm.

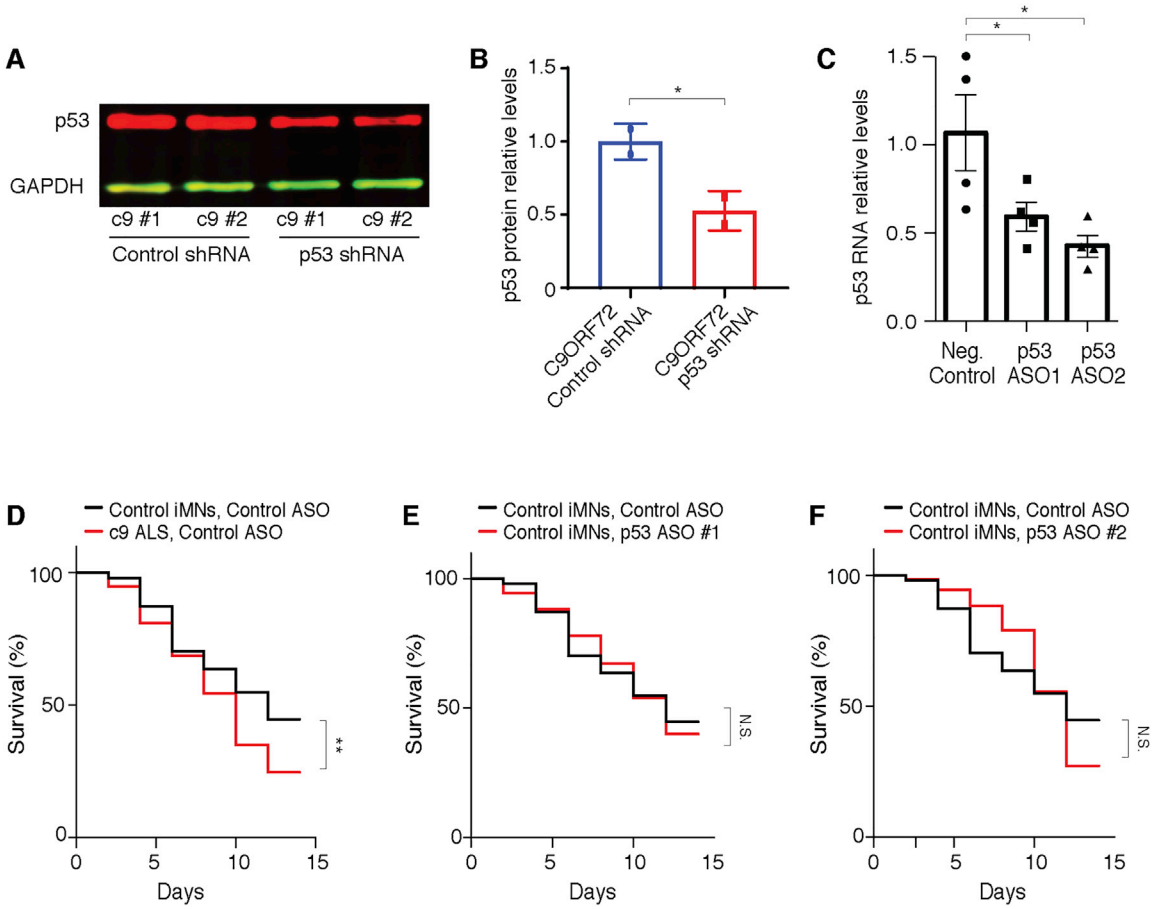

Figure S7. p53 reduction modifies neurodegeneration in C9-ALS models, related to Figure 6

(A and B) p53 shRNA lentiviral transduction decreases p53 levels in iPSC-derived neurons differentiated from two independent *C9orf72* mutation carriers. Quantification of p53 levels by immunoblotting and normalized to actin. Graphs show mean ± SEM (t test; *p < 0.05).

(C–F) Relative p53 RNA expression in iMNs treated with 9 μM negative control or p53 ASOs for 24 hours, as determined by RT-PCR. (C) Mean ± s.e.m., One-way ANOVA. n = 4 biological replicates per group. *p < 0.05. The c9ALS patient-derived iMNs showed reduced survival (D). Survival of CTRL iMNs was not affected by p53 ASO treatment; log-rank Mantel-Cox test; n = 3 independent iMN lines with n = 195 iMNs per condition per treatment; **p < 0.01, N.S. not significant (E and F).